Ph. D. DISSERTATION

STABILITY ANALYSIS OF PEROVSKITE SOLAR CELLS AND LIGHT-EMITTING DIODES

페로브스카이트 태양전지 및 발광다이오드의 수명 안정성 연구

BY

HYUNHO LEE

AUGUST 2018

DEPARTMENT OF
ELECTRICAL AND COMPUTER ENGINEERING
COLLEGE OF ENGINEERING
SEOUL NATIONAL UNIVERSITY

STABILITY ANALYSIS OF PEROVSKITE SOLAR CELLS AND LIGHT-EMITTING DIODES

페로브스카이트 태양전지 및 발광다이오드의 수명 안정성 연구

지도교수 이 창 희

이 논문을 공학박사 학위논문으로 제출함

2018 년 8 월

서울대학교 대학원

전기·컴퓨터 공학부

이 현 호

이현호의 공학박사 학위논문을 인준함

2018 년 8 월

위 원 장 : _____ (인)

부위원장 : _____ (인)

위　　원 : _____ (인)

위　　원 : _____ (인)

위　　원 : _____ (인)

Abstract

STABILITY ANALYSIS OF PEROVSKITE SOLAR CELLS AND LIGHT-EMITTING DIODES

HYUNHO LEE

DEPARTMENT OF

ELECTRICAL AND COMPUTER ENGINEERING

COLLEGE OF ENGINEERING

SEOUL NATIONAL UNIVERSITY

Perovskite is one of the most promising material for next generation optoelectronic applications. The organic-inorganic hybrid ABX_3 (A: larger cation, B: smaller cation, X: halide anion) structure exhibit semiconductor to metal transition characteristics with dimensionality. 2D to 3D phase transition of perovskite structure provides wide range of bandgap which promises the various optoelectronic characteristics for device applications. An ionic perovskite crystal shows high absorption coefficient (1.5×10^4 cm^{-1} at 550 nm for $CH_3NH_3PbI_3$) which indicates the penetration depth of 550 nm wavelength light is about 0.66 μm. This superior absorption characteristic enables

perovskite to be applicable for thin film solar cells. Since the first perovskite solar cell was reported in 2009, power conversion efficiency of perovskite solar cells has been drastically improved. And now perovskite solar cells are the most promising candidate for the next generation sustainable energy source. Furthermore, color-tunability by bandgap tuning of perovskite brings various applications in light sources such as light-emitting diodes. The full width half maximum of electroluminescence of perovskite light-emitting diodes shows only about 20 nm. This high color purity has strong advantages over commercialized light sources such as organic light-emitting diodes.

Perovskites are easily decomposed by polar solvents such as dimethylformamide (DMF), dimethyl sulfoxide (DMSO), ethanol, and water. Under humid conditions, perovskite shows significant degradation process which hinders the lifetime and stability of perovskite optoelectronic devices. To be successful as a next generation energy sources or light sources, perovskite should overcome stability issues. Compositional change of perovskite was studied by incorporating small amount of cesium or formamidinium. Structural development was also studied to enhance the stability of perovskite optoelectronic devices. Although many researches have been made to improve stability of perovskite optoelectronic devices, perovskite optoelectronic devices still suffer from the degradation even under the encapsulated condition. Hence, the systematic study about degradation source and underlying degradation mechanism of perovskite optoelectronic devices is essential and has to be preceded to realize the commercialization of perovskite optoelectronic devices.

In this thesis, systematic studies on degradation mechanism of both perovskite solar cells and perovskite light-emitting diodes are discussed. In terms of device configuration in perovskite optoelectronic devices used herein, an inverted structure, the electrons are collected or injected by the top metal electrode, and holes are collected or injected by the bottom electrode – indium tin oxide (ITO), is employed.

The first part is about the perovskite solar cells. Here, direct evidence for ion-diffusion-induced interfacial degradation in inverted perovskite solar cells is presented. Over 1000 hours, perovskite solar cells show degradation, especially with respect to the current density and fill factor. The Ag electrode is peeled off and re-evaporated to investigate the effect of the Ag/[6,6]-phenyl C71 butyric acid methyl ester (PCBM) interfacial degradation on the photovoltaic performance at days 10 (240 hours), 20 (480 hours), 30 (720 hours), and 40 (960 hours). The power conversion efficiency increases after the Ag electrode restoration process. While the current density shows a slightly decreased value, the fill factor and open-circuit voltage increase for the new electrode devices. The decrease in the activation energy due to the restored Ag electrode induces recovery of the fill factor. The diffused I^- ions react with the PCBM molecules, resulting in a quasi n-doping effect of PCBM. Upon electrode exchange, the reversible interaction between the iodine ions and PCBM causes current density variation. The disorder model for the open-circuit voltage over a wide range of temperatures explains the open-circuit voltage increase at every electrode exchange. Finally, the degradation mechanism of the inverted perovskite solar cell over 1000 hours is described under the proposed recombination system.

The second part is about the perovskite light-emitting diodes. The fabrication process to obtain compact and pin-hole free perovskite film is critical issue in the research field of perovskite light-emitting diodes. Here, sequential deposition method to fabricate perovskite light-emitting diodes is demonstrated. Lead bromide solution and methyl ammonium bromide solution are sequentially spin coated and annealed, resulting in compact and pin-hole free perovskite film. Perovskite light-emitting diodes exhibit 67,557 cd/m^2 with high external quantum efficiency 2.02%. Furthermore, the origin of perovskite light-emitting diode degradation is investigated. Direct evidence of ion diffusion from perovskite layer under device operation is

observed. Based on the electro-chemical interaction between degradation sources and Al electrode, the degradation mechanism of sequentially deposited perovskite light-emitting diodes is proposed.

This thesis demonstrates practical approaches to analyze degradation mechanism of perovskite optoelectronic devices. The novel ion-diffusion induced degradation mechanism especially on the metal electrode interfacial layer would expect to contribute further improvement on lifetime of perovskite optoelectronic devices.

Contents

Chapter 2 Experimental Methods   15

x

List of Figures

xiii

xvii

List of Tables

xx

Chapter 1

Introduction

1.1 Perovskite Solar Cells

Organometal halide perovskite solar cell (PSC) was firstly reported by Kojima *et al* in 2009.[1] 3.8% of power conversion efficiency (PCE) was reported with the iodine based perovskite. Although the PCE was relatively lower than that of commercialized solar cells such as silicon solar cells, the long range of absorption spectra (from 300 nm to 800 nm) and high absorption coefficient (α ~1.5×10^4 at 550 nm) exhibited the large room for the improvement of photovoltaic characteristics. The first type of perovskite solar cells adopted the structure of dye-sensitized solar cells (DSSCs). Organic electrolyte solution fills the gap between perovskite absorber and Pt counter electrode. This liquid state electrolyte was unfavorable due to the bad device stability. In 2012, thin solid-state PSC was reported by Kim *et al*.[2] PCE reached almost 10% (9.7%) with improved device stability (PCE over 8% under 500 hour degradation).
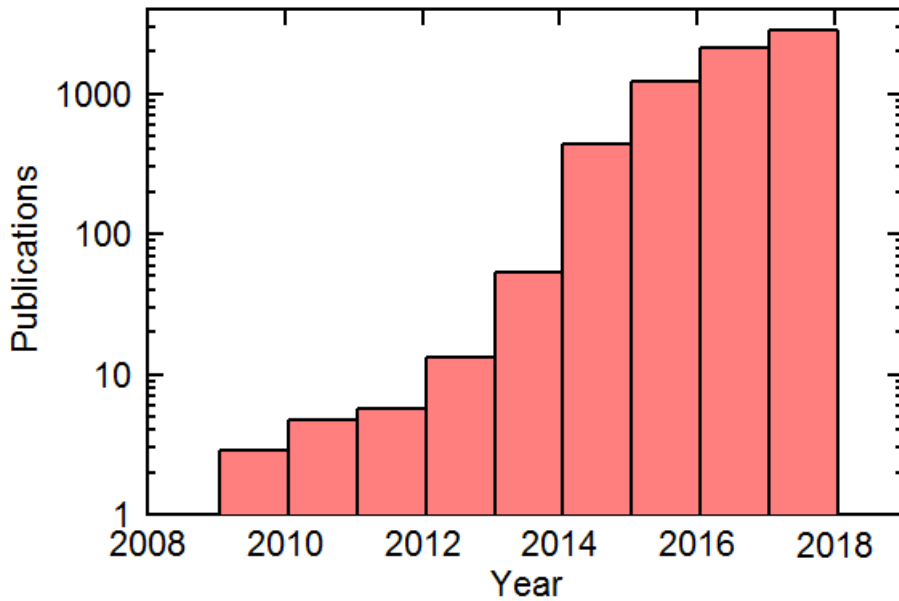
Figure 1.1 Number of publication in the research field of perovskite solar cells.
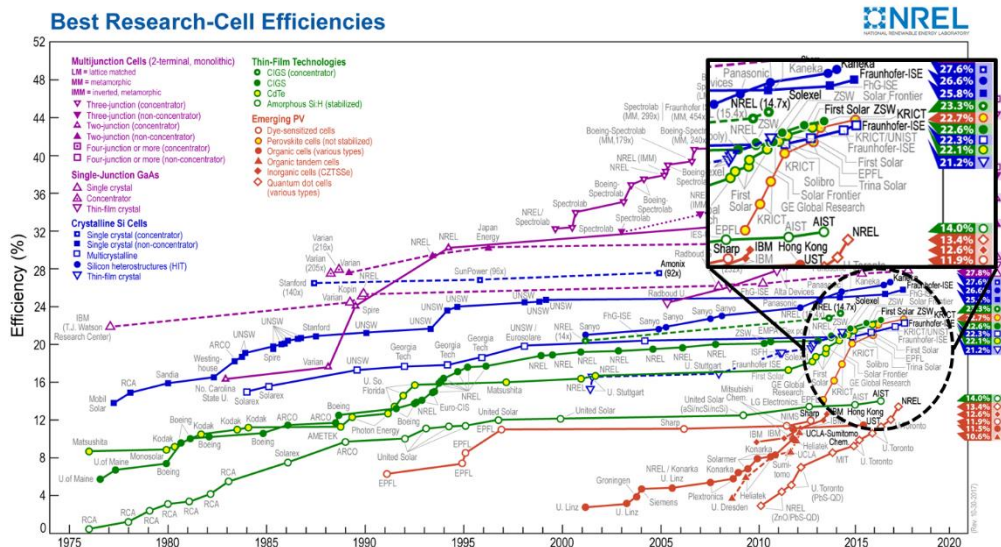
Figure 1.2 Best research-cell efficiencies from National Renewable Energy Laboratory (NREL).

The solid-state PSC exhibited promising photovoltaic characteristics for the next generation solar cells, result in boosting the research field of PSCs. The number of publications in the research field of PSCs increased exponentially as shown in Figure 1.1. PCE of PSCs increased rapidly as shown in Figure 1.2. The key factor to increase PCE of PSCs is the morphological control of perovskite film. The solution processed perovskite film showed many pin-holes during crystallization phase which induced absorption losses and shunt path between charge transport layers.[3] Compact and pin-hole free perovskite films could be acquired by sequential deposition method and anti-solvent engineering method.[4-5] The sequential deposition method represents the perovskite film fabrication technique where lead iodide (PbI_2) and methylammonium iodide (MAI) solutions are deposited sequentially. The pre-coated PbI_2 ensures the fine film formation and the inter-mixing of MAI and PbI_2 forms the compact perovskite film. The anti-solvent engineering method represents the spin-coating technique where anti-solvents (chlorobenzene, chloroform, toluene, ether) are dripped during the spin-coating process of perovskite solution. These anti-solvents induce different nucleation kinetics of perovskite solution and their residuals have unique influence on perovskite crystal growth, results in fine perovskite film. Based on development of film fabrication method and chemical compositional optimization, PCE of PSCs exceeded 22%. The solution-processed high performance thin film PSCs are expected to substitute silicon solar cells within years. However, the stability issue is the most urgent problem in the research field of PSCs which will be discussed in subsequent chapter 1.3.

1.2   Perovskite Light-Emitting Diodes

The first perovskite light-emitting diode (PeLED) was reported in 2014 with the external quantum efficiency (EQE) of 0.1%.[6] The pure green and red colored emission exhibited full width half maximum of 35 nm. Moreover, color tunability by controlling compositional variation of perovskite solution exhibited strong advantage over competing emerging light sources such as organic light-emitting diodes (OLED) and quantum dot light-emitting diodes (QDLED). The morphological control of perovskite film is also important for the light-emission properties. Electro-luminance (EL) of PeLEDs was dynamically improved by introducing anti-solvent pinning method for the perovskite film fabrication.[7] Anti-solvent pinning method is almost similar to anti-solvent engineering of PSCs. Small amount of anti-solvent (toluene) with small molecule organic material is dripped during the perovskite solvent spin-coating process. This anti-solvent pinning method ensures compact and pinhole free perovskite film. The grain size of the perovskite film exhibited less than 100 nm which confines electrons and holes effectively. Spatially confined free electrons and holes induced effective radiative recombination which showed improvement of the light emission properties. As a result, EQE of PeLEDs had reached 8%. Further improvement of PeLEDs were made by introducing surface passivation of perovskite film and compositional variation of perovskite solution.[8-10] 14.36% EQE was achieved and there are still room for the further improvement of PeLEDs. Although, the improvement of emission band property and efficiency are close enough to be commercialized as a light source, operational stability of PeLEDs should be improved for the industrial applications. Many degradation mechanisms were reported in the research field of perovskite solar cells. Oxygen and humidity induced deterioration of perovskite film or ion diffusion induced interfacial degradation were the main

degradation sources of the PSCs. Because forward bias of voltage to operate PeLED causes electrical field induced degradation, systemic analysis on the degradation mechanism of PeLEDs is required. The stability issue of PeLEDs will be covered on the subsequent chapter 1.3.

1.3   Stability Issues in Perovskite Optoelectronic Devices

Organometal halide perovskites have weak property to humidity. As mentioned previously, perovskites are easily dissolved into polar solvents such as DMF, DMSO, or water. Decomposition of perovskite film under ambient air condition causes poor device stability of perovskite optoelectronic devices. Because perovskites are composed of organic, halide, and metal parts, degradation comes from the intermixing behavior of these by-products. Perovskite optoelectronic devices have several buffer layers such as electron transport layer (ETL), hole transport layer (HTL), and metal electrode. Obviously, decomposed perovskite by-products have defective relationship with buffer layers which accelerates device degradation. Hence, it is very important to understand not only degradation mechanism of perovskite, but also interfacial degradation mechanism between perovskite by-products and buffer layers.
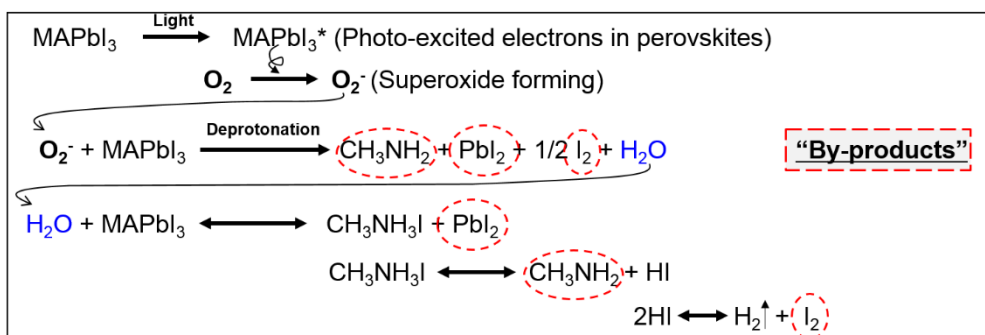
Figure 1.3 Perovskite decomposition mechanism and the remaining by-products under ambient air and light exposure condition.

1.3.1 Stability Issues in Perovskite Solar Cells

The basic structure for the most widely used and studied perovskite is $CH_3NH_3PbI_3$ ($MAPbI_3$). Before we introduce the environmental stability of PSCs, we need to address why we chose inverted structure in our study. In the PSC system, ion migration depends on applied electric field exist due to halide related unique characteristic of perovskite.[11-12] This ion migration is known as causing anomalous hysteresis in PSCs. The current density–voltage (J-V) hysteresis indicates that the J-V curves have different shape depend on the scan direction.[13] Hysteresis in PSCs causes difficulties in quantitative analysis of device physics. The normal structured PSCs exhibited larger hysteresis than the inverted structured PSCs, especially titanium dioxide (TiO_2) based planar PSCs. On the other hand, inverted structured PSCs, mostly based on poly(3,4-ethylenedioxythiophene)-poly(styrenesulfonate) (PEDOT:PSS), exhibited hysteresis-free J-V characteristics. Thus, reliable analysis on device physics was performed in our system based on inverted structure PSCs.

Under ambient air condition, perovskites are decomposed into CH_3NH_2, PbI_2, I_2, and H_2O as shown in Figure 1.3 and 1.4.[14-15] These decomposed by-products accelerate degradation process of perovskite solar cells. To enhance the device lifetime against humidity, mixed halide system was introduced.[16] Smaller Br atoms substitute larger I atoms which induced reduction of the lattice constant, resulted in improved stability. In this direction of perovskite compositional variation studies, organic cation (CH_5N_2 (FA)) and metal cations (Cs, Rb) were introduced to perovskite solar cells. Saliba et al reported the mixing of triple cation (MA, FA, Cs) suppresses phase impurities and induces uniform perovskite grains yielding operational stability (PCE degradation to 90% of initial value) over 250 h under 1 sun illumination condition.[17] The interface modification (HTL, ETL) was also investigated. In the inverted PSCs, due to its
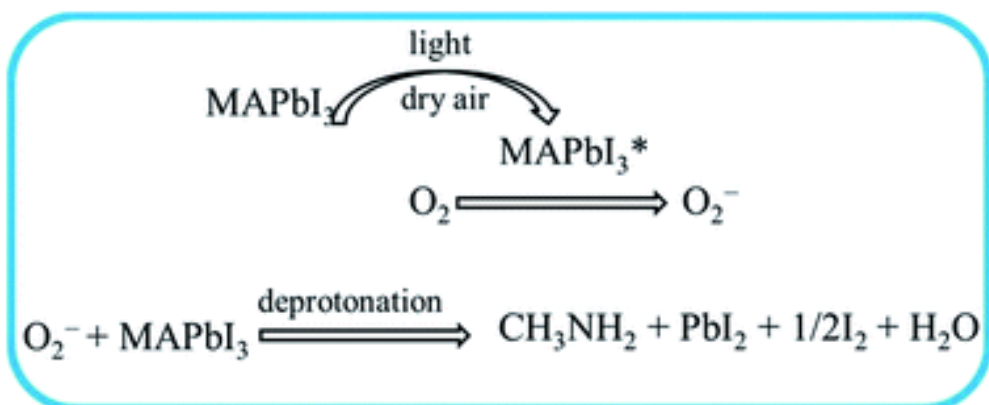
Figure 1.4 Perovskite decomposition mechanism under ambient air and light exposure condition.[14]

hydrophilic and acidic nature, PEDOT:PSS provides reasons for low lifetime of perovskite optoelectronic devices. Instead of PEDOT:PSS, stable p-type metal oxide NiO_X was introduced which enhanced device stability dramatically.[18] Brinkmann et al inserted tin oxide (SnO_X) for additional electron-extraction layer by atomic layer deposition method.[19] Dense oxide layer was formed to prevent gas permeation which effectively hinders the ingress of moisture towards the perovskite film. Moreover, the decomposition of perovskite layer by elevating temperature was diminished. The investigation on the metal electrode for the device stability was also reported. In the PSCs, Al electrode shows fast oxidization process under air exposure. Pin-holes are created which accelerate device degradation.[19-20] Zhao et al reported the possibility of Cu electrode for the metal cathode.[21] Cu electrode exhibited advantageous feature against humidity exposure. Over 800 hours, PCE was maintained as its original level. Carbon electrode was used to enhance the device stability.[22] Carbon electrode has no severe reaction with the halides from the degraded perovskite layer. Moreover, dense carbon electrode could block the permeation of oxygen or humidity under ambient air

condition. As a result, operational stability (PCE degradation to 90% of initial value) over 600 hours was achieved.

Degradation kinetics for each perovskite constituent layers are combined to accelerate total device degradation of PSCs. Perovskites have unique degradation mechanism with the halide ions. Hence, it is very important to understand the role of halides during the degradation phase of PSCs. The influence of perovskite by-products on the buffer transport layers and metal electrode should be investigated for the clear understanding of PSC degradation mechanism. Degradation mechanism on the electrode interfacial layer will be discussed in *Chapter 3*.

1.3.2   Stability Issues in Perovskite Light-Emitting Diodes

Bromide base green emissive perovskites ($CH_3NH_3PbBr_3$) are the most widely studied structure for the light-emission application. Forward bias over 3V should be biased on the PeLED to operate the device. This forward bias would put another degradation factor to the light-emitting devices which is different from the solar cells. Unlike the PSCs, researches about the PeLED stability were inadequate. Figure 1.5 shows the number of publications in the research field of PeLED as a key word "Stability".
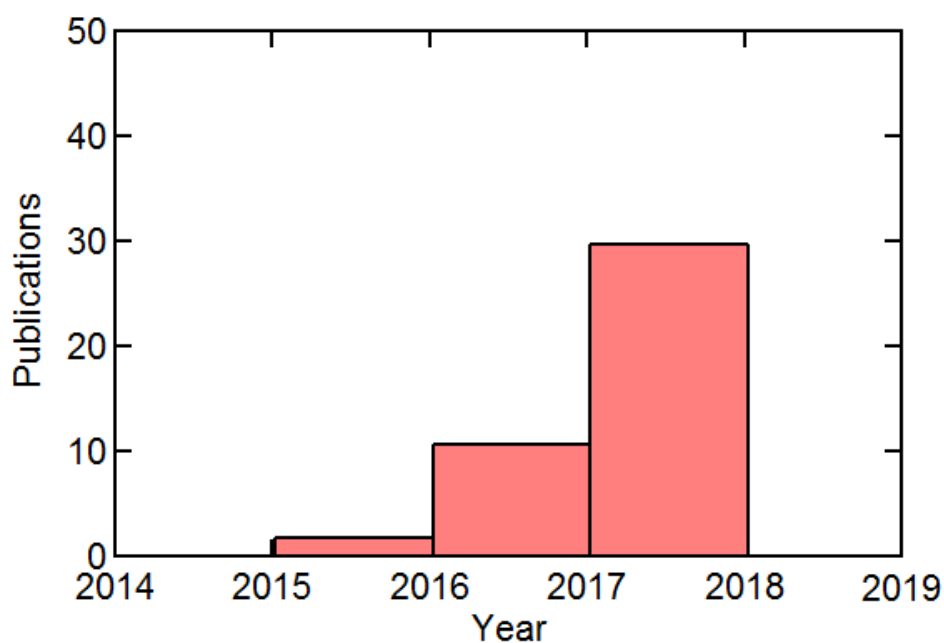
Figure 1.5 The number of publications on perovskite light-emitting diodes about stability.

Only about 30 articles dealt the stability issue of PeLEDs in 2017. The operational lifetime of PeLED was very poor in the early stage of PeLED research. T_{66} (luminance degradation to 66% of initial value) lifetime was only 4 min.[23] The development of
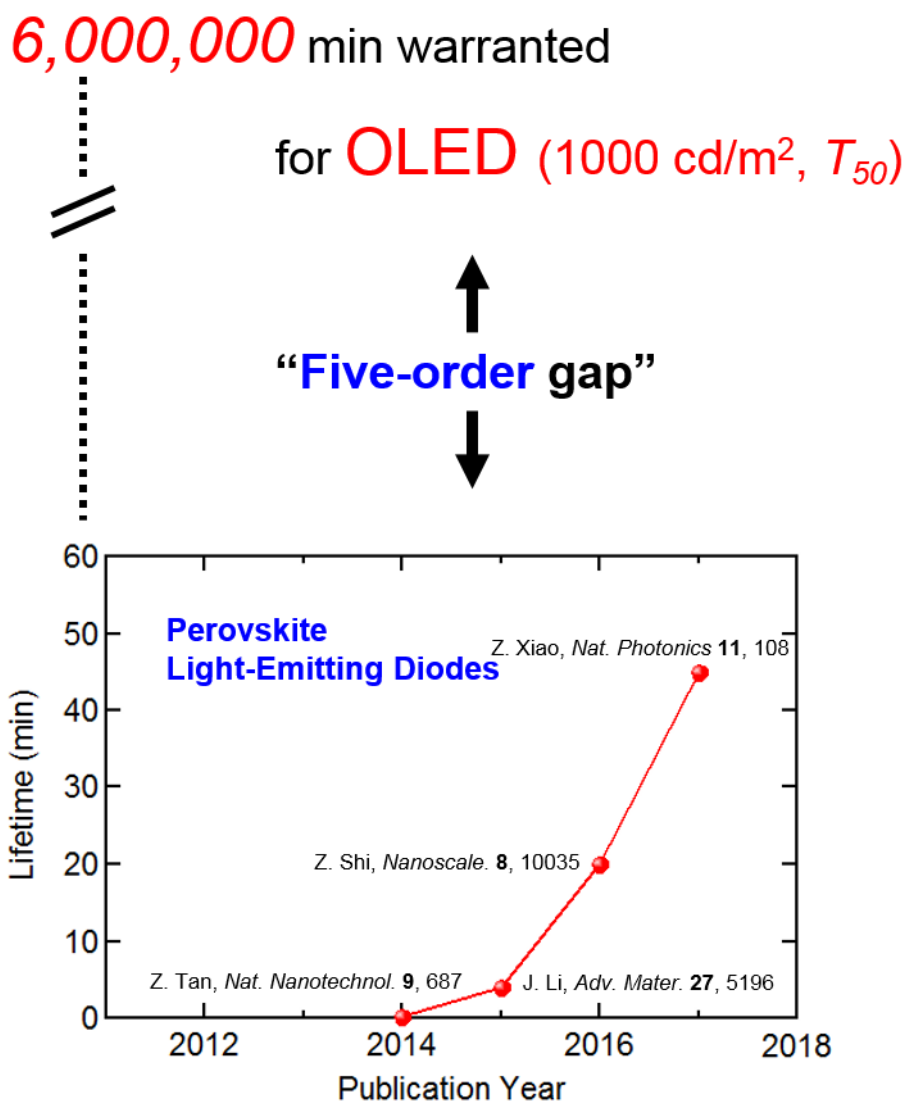
Figure 1.6 The development of the T_{50} lifetime of the PeLEDs.

the T_{50} (decay time to 50% of the initial luminance) lifetime of the PeLEDs is shown in Figure 1.6. The most important factors in the degradation of PeLED are joule heating and ion diffusion. During the light emission, the radiative and non-radiative recombination of electron-hole pair produce heat which could damage the perovskite

film and induce decomposition of perovskite film. This decomposition of perovskites creates halide by-product. The forward bias electric field accelerate halide ion diffusion along the electric field direction. Very few degradation mechanisms have been reported up to date. We would expect following degradation study contributes to the improvement of the device stability. Degradation mechanism of PeLEDs will be discussed in *Chapter 4*.

1.4   Outline of Thesis

This thesis is divided into five chapters.

In the introduction of *Chapter 1*, brief overview with development history of perovskite solar cells and light-emitting diodes are explained. Moreover, the stability issue on both perovskite solar cells and light-emitting diodes is emphasized.

Chapter 2 describes the experimental methods for both perovskite solar cells and light-emitting diodes. The basic principles of characterization of perovskite solar cells and light-emitting diodes are explained. The detailed experimental measurement conditions are also described.

In *Chapter 3*, the novel ion-diffusion induced degradation mechanism of perovskite solar cells are investigated. The Ag electrode restoration process exhibit recovery of PCE. The low temperature analysis give an explanation about the variation of each solar cell parameters with respect to degradation time.

In *Chapter 4*, the efficient perovskite light-emitting diodes are fabricated by sequential deposition method. The ion-diffusion induced degradation mechanism is investigated. The *in-situ* observation of perovskite morphological degradation with electro-chemical device analysis provide novel degradation mechanism of perovskite light-emitting diodes.

Chapter 5 summarizes the results and concluding remarks of this thesis are given.

Chapter 2

Experimental Methods

2.1 Materials

PEDOT:PSS (AI4083) was purchased from Heraeus. Dimethylformamide (DMF), dimethyl sulfoxide (DMSO), isopropyl alcohol (IPA), chloroform (CF) and chlorobenzene (CB) were purchased from Sigma-Aldrich. All materials were used as received without any purification.

2.1.1 Perovskite Solar Cells

Methylammonium iodide (MAI, 99.5%) was purchased from Xian Polymer Light Technology. Lead iodide (PbI_2, 99.9985%) was purchased from Alfa Aesar. PCBM was purchased from 1-Material. All materials were used as received without any purification.

2.1.2 Perovskite Light-Emitting Diodes

Methylammonium bromide (MABr, 99.5%) was purchased from Xian Polymer Light Technology. Lead bromide (PbBr$_2$, 99.999%) was purchased from Alfa Aesar. 2,2′,2″-(1,3,5-Benzinetriyl)-tris(1-phenyl-1-H-benzimidazole) (TPBi) was purchased from OSM. Polyvinylpyrrolidone (PVP) was purchased from Sigma-Aldrich. All materials were used as received without any purification.

2.2 Device Fabrication Methods

2.2.1 Perovskite Solar Cells

ITO-patterned glass substrates were separately cleaned with acetone, IPA, and deionized water. Substrates were treated with UV-ozone for 15 min. PEDOT:PSS was filtered (PTFE, 0.45 μm) and spin-coated (3500 rpm, 30 s). PEDOT:PSS-coated substrates were annealed at 130 °C for 20 min. Then, the substrates were transferred to an Ar-filled glove box for perovskite deposition. A two-step perovskite deposition method was used. A 1.2 M PbI$_2$ solution was prepared in a DMF/DMSO (9:1) mixed solvent. The PbI$_2$ solution was annealed and stirred overnight at 70 °C. MAI was dissolved in IPA to create a MAI solution (50 mg/ml). Both the PbI$_2$ and MAI solutions were filtered (PTFE, 0.45 μm) before using. The PbI$_2$ solution was spin-coated (3000 rpm, 30 s). The PbI$_2$-coated substrates were dried for 3 min. Then, the MAI solution was immediately spread on the PbI$_2$ film and spin-coated (3000 rpm, 30 s). The light brownish colored perovskite films were annealed at 60 °C for 1 min and 100 °C for 120 min. The perovskite-coated substrates were cooled to room temperature, and PCBM (23 mg/ml) was spin-coated (2000 rpm, 30 s). Then, the

substrates were transferred to a dry box (relative humidity under 15%) and kept overnight. Finally, the 100 nm Ag electrode was thermally evaporated under 10^{-6} Torr.

2.2.2　Perovskite Light-Emitting Diodes

Preparation of PVP and perovskite solution. A 0.5 ~ 1.5 wt% PVP was prepared by dissolving PVP in DMSO. A 0.3 ~ 1.0 M $PbBr_2$ solution was prepared by dissolving $PbBr_2$ in DMSO. A 7 ~ 15 mg/ml MABr solution was prepared by dissolving MABr in IPA. For the one-step perovskite film fabrication, 40 wt% perovskite solution with (1.05:1 molar ratio of MABr and $PbBr_2$ in DMSO) was used. All solutions were stirred overnight and kept in room temperature. All solutions were filtered (PVDF, 0.45 μm) before using.

Device fabrication. ITO-patterned glass substrates were cleaned by acetone, IPA, and deionized water. UV-ozone was treated before PEDOT:PSS spin-coating. PEDOT:PSS was filtered (PTFE, 0.45μm), spin-coated (3500 rpm, 30 s), and annealed (130 ℃, 20 min). The PEDOT:PSS coated substrates were transferred to Ar-filled glovebox. A various concentration of PVP solution was spin-coated (2000 rpm, 60 s) and annealed (140 ℃, 15 min). On the PVP coated substrates, sequential deposition of perovskite film was conducted. A various concentration of $PbBr_2$ solution was spin-coated (3000 rpm, 60 s) and annealed (70 ℃, 10 min). To form the perovskite film, a various concentration of MABr solution was spread on $PbBr_2$ coated substrate rapidly. The spread MABr solution was loaded for few minutes (1 ~ 2 min), spin-coated (3000 rpm, 30 s), and annealed (70℃, 1 min and 100 ℃, 30 min). For the one-step perovskite film, 40 wt% perovskite solution was spin-coated (500 rpm, 10 s and 2800 rpm 90 s). Before the end of spin-coating (23 s before), 0.1 wt% of TPBi in CF solution was poured. Finally, TPBi (40 nm), LiF (1 nm), and Al (130 nm) were

thermally evaporated under 10-6 Torr. The active (emission) area where ITO and Al cross was 0.0196 cm2. The best performance SDPeLED was fabricated from the solution concentration of PVP (0.5 wt%), $PbBr_2$ (0.5 M), and MABr (10 mg/ml). The complete devices were encapsulated for measuring light-emitting performances.

2.3   Device Characterization of Perovskite Solar Cells

2.3.1   Solar Cell Performance Parameters

In order to determine the performance and electrical characteristics of the photovoltaic devices, current density-voltage (*J-V*) measurements are performed under the illumination of solar simulator which can provide approximating natural sunlight. A typical *J-V* characteristic of a solar cell is shown in Figure 2.1.
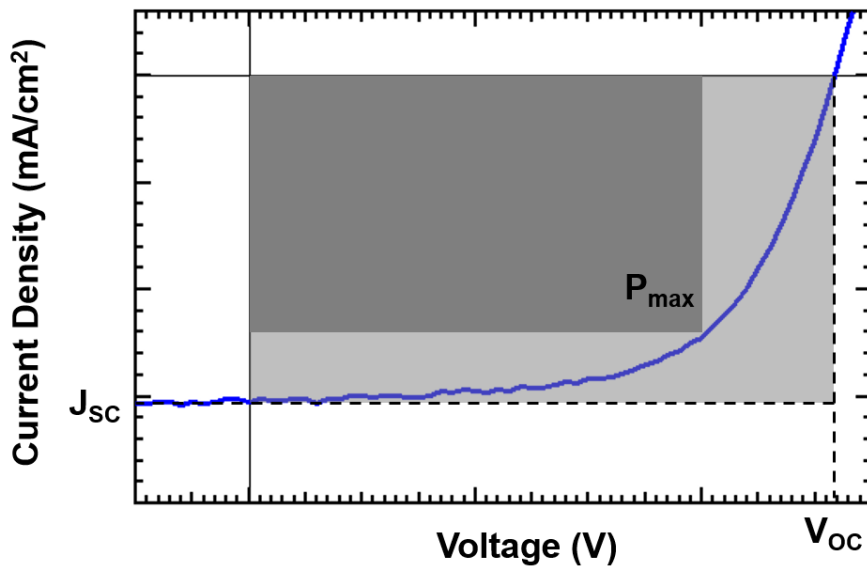
Figure 2.1 Current density-voltage (*J-V*) curve of solar cell.

While the power from the solar cell is zero at the operating points of both current density (J_{SC}) and open-circuit voltage (V_{OC}), there is a point where the solar cell can deliver its maximum power (P_{max}) to an external load. The fill factor, FF is defined as the ratio of the maximum power generated from the solar cell to the product of V_{OC} and J_{SC}, which is shown in equation (2.1).

19

$$FF = \frac{P_{\text{Max}}}{J_{\text{SC}} \times V_{\text{OC}}} \tag{2.1}$$

The FF can also be graphically defined as the ratio of the area of the maximum possible largest rectangle (dark grey region in Figure 2.1) which fits in the *J-V* curve, to the rectangle formed with V_{OC} and J_{SC}. The ideal value for FF is unity (100%), if all the generated charge carriers are extracted out of a device without any losses.

The efficiency of a solar cell, which is defined as the fraction of incident power converted to electricity, is the most commonly used parameter to show the performance of solar cells. The power conversion efficiency, *PCE*, is given by

$$PCE\,(\%) = \frac{\text{Electric Power}}{\text{Light Power}} = \frac{V_{\text{OC}} \times J_{\text{SC}} \times FF}{P_{\text{light}}} \times 100\,(\%) \tag{2.2}$$

where P_{light} is the incident power of light. The efficiency is needed to be measured under the standard test conditions for comparing performances from one to another, because it has a dependence on spectrum and intensity of incident sunlight. The standard condition includes an irradiance of 1 sun (100 mW/cm^2) with an air mass 1.5 global (AM 1.5G) solar spectrum as shown in Figure 2.2.
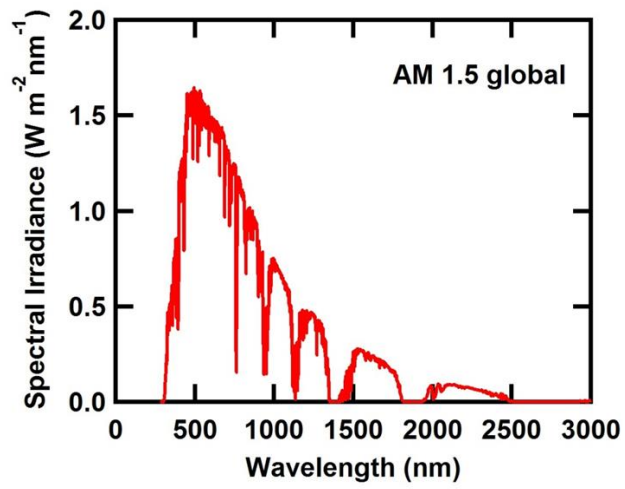
Figure 2.2 AM 1.5G spectral distribution of solar irradiation.

Figure 2.3 300 W Xenon lamp solar simulator.

2.3.2 Current Density-Voltage Characteristics Measurement

J-V curves were measured by a 300 W Xenon lamp based solar simulator (Newport 91160A, Figure 2.3) and a Keithley 237 source measurement unit under AM 1.5G 1-sun illumination (100 mW/cm^2). The light intensity was controlled by an optical density filter. The temperature was controlled by a LakeShore 331 temperature controller and a Suzuki Shokan helium compressor unit (C100G).

2.3.3 Temperature Controlled Experiment

The trapping nature of the carrier dynamics exhibits an Arrhenius relation between J_{SC} and the temperature as following,

$$J_{SC}(\text{T}, P_{light}) = J_0(P_{light}) \times \exp(-\frac{\Delta}{K_B T}) \tag{2.3}$$

where *T* is the temperature, P_{light} is the light intensity, J_0 is the pre-exponential factor, determined by photogeneration, recombination, and transport of carriers, K_B is the Boltzmann constant, and *Δ* is the activation energy. The activation energy is denoted as the energetic depth of the shallow trap states. Photogenerated charges need *Δ* energy to be extracted efficiently to both electrodes. By taking the neutral log "*ln*" to both side of equation 2.3, following equation is derived.

$$ln J_{SC}(\text{T}, P_{light}) = -\frac{\alpha \Delta}{K_B T} \tag{2.4}$$

Where *α* is the constant. The relationship "*lnJ$_{SC}$−1/T*" can be plotted and by taking the slope of the "*lnJ$_{SC}$−1/T*" relationship, the activation energy *Δ* can be calculated for each light intensities.

2.4 Device Characterization of Perovskite Light-Emitting Diodes

2.4.1 Current Density-Voltage-Luminance Measurement

The current-voltage (I-V) characteristics were measured with a Keithley 236 source measurement unit, while the electroluminescence was measured with a calibrated Si photodiode (Hamamatsu, S5227-1010BQ) with a size of 10 mm × 10 mm placed at an angle normal to the device surface, assuming that the device was a Lambertian source. To detect a turn-on voltage of light-emitting diodes, we use an ARC PD438 photomultiplier tube (PMT) with the Keithley 236 source measurement unit. The electroluminescence (EL) spectra and the Commission Internationale de L'Eclairage (CIE) color coordinates were measured with a Konica-Minolta CS-1000A spectroradiometer. The luminance and efficiency were calculated from the photocurrent signal of photodiode with a Keithley 2000 multimeter, and corrected precisely with the luminance from CS-2000.

The chromatic characteristics were calculated from EL spectra measured by the CS-2000 spectrometer using the CIE 1931 color expression system. The tristimulus values XYZ can be calculated by following equations,

$$X = K_m \int_0^\infty \bar{x}(\lambda)P(\lambda)d\lambda \tag{2.5}$$

$$Y = K_m \int_0^\infty \bar{y}(\lambda)P(\lambda)d\lambda \tag{2.6}$$

$$Z = K_m \int_0^\infty \bar{z}(\lambda)P(\lambda)d\lambda \tag{2.7}$$

where, P(λ) is a given spectral power distribution of emissive source, $\bar{x}$, $\bar{y}$ and $\bar{z}$ are the CIE standard color matching functions (see Figure 2.4) and Km is the

23

weighing constant (683 lm W^{-1}). From the tristimulus values, the CIE color coordinates calculated by following equations,

$$x = \frac{X}{X+Y+Z} \tag{2.8}$$

$$y = \frac{Y}{X+Y+Z} \tag{2.9}$$

$$z = \frac{Z}{X+Y+Z} \tag{2.10}$$

Any color can be plotted on the CIE chromaticity diagram.
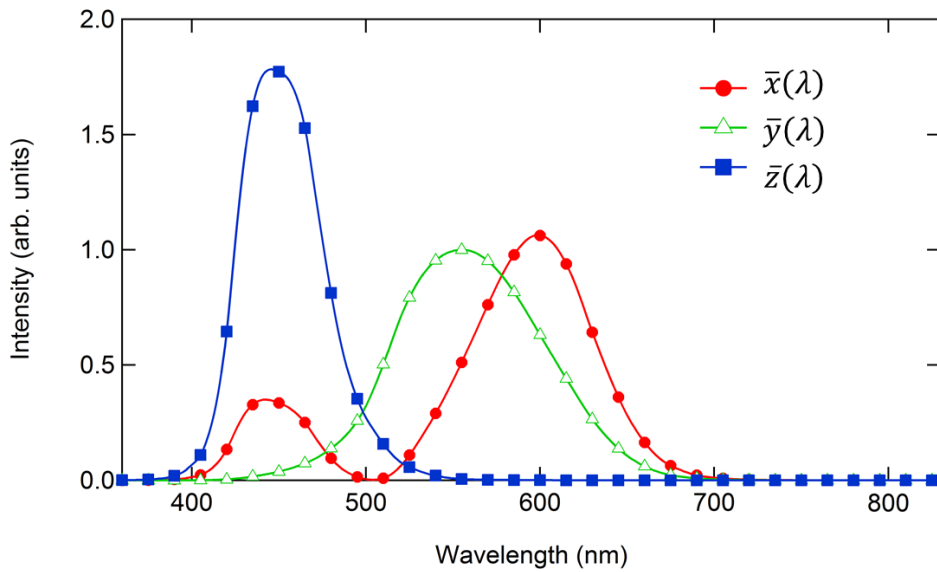
Figure 2.4 CIE standard observer color-matching functions.

2.4.2 Efficiency Calculation Methods

To evaluate the emission properties of light-emitting diodes, the commonly employed efficiencies are the external quantum efficiency (EQE), the luminous efficiency (LE) and the power efficiency (PE).

The external quantum efficiency can be defined by the following equation.

$$\text{EQE} = \frac{number\ of\ emitted\ photons}{number\ of\ injected\ electrons}(\%) \tag{2.11}$$

Typically, light is emitted into the half plane due to the metal contact. Without any modification for increasing out-coupling efficiency, over 80% of the emission can be lost to internal absorption and wave-guiding in a simple planar light-emitting device.

Since human eye has different spectral sensitivity in visible area, the response of the eye is standardized by the CIE in 1924. The luminous efficiency weighs all emitted photons according to the photopic response of human eye. The difference is that EQE weighs all emitted photons equally. LE can be expressed by the following equation.

$$\text{LE} = \frac{luminance}{current\ density}(cd\ A^{-1}) \tag{2.12}$$

The luminance value (cd m^{-2}) can be easily measured by the commercial luminance meter (CS-2000 in this thesis).

The power efficiency is the ratio of the lumen output to the input electrical power as follows,

$$\text{PE} = \frac{luminous\ flux}{electrical\ power}(lm\ W^{-1}) \tag{2.13}$$

The EQEs can be useful to understand the fundamental physics for light emission mechanism, while the PEs can be useful to interpret the power dissipated in a light-emitting device when used in a display application

2.5 Other Characterization Methods

2.5.1 UV-Visible Spectroscopy

The UV-vis absorbance was measured by U-2900 spectrophotometer (HITACHI). The absorbance measurement range was from 350 nm to 900 nm. The glass substrate was set as a baseline for the measurement.

2.5.2 Time of Flight Secondary Ion Mass Spectrometry

TOF-SIMS was measured by ION-TOF (Germany). Analysis gun was activated with Bi+ 30 kV at 1 pA with area of 70 x 70 μm^2. Sputter gun was activated with Cs+ 500 eV at 45 nA with area of 230 x 230 μm^2. Pulsing time was 150 μs with 3 x 1012 ions/cm^2 PIDD (ion dose density limit). The negative ions were used in this thesis. Al$^-$ and Ag$^-$ ions were used to detect the Al and the Ag electrodes. S$^-$ and SO2$^-$ ions were used to detect PEDOT:PSS layers. I$^-$, Br$^-$, Br$_2^-$, and Pb$^-$ ions were used to detect perovskite layers. C$^-$ ions were used to detect PCBM layer. CH$^-$ ions were used to detect TPBi layer. Samples were kept in the high vacuum condition before the measurements.

2.5.3 Field Emission Scanning Electronic Microscopy

Field-emission SEM was taken by SIGMA (Carl Zeiss). Cross sectional SEM using focused ion beam (FIB) was taken by AURIGA (Carl Zeiss). 5 to 10 nm of Pt was coated on the perovskite film to take the surface SEM image. 20 to 30 nm of Pt was coated on the perovskite film to take the cross sectional SEM image. To prevent the morphological distortion during the FIB process, additional Pt protecting layer was

deposited. The substrates were tilted 56° to take the cross sectional SEM images. Because the glass substrates were used in the measurement, the edges of the substrates were sealed with the carbon tape to prevent the electrical leakage from the SEM machine.

2.5.4   Raman Spectra

The Raman spectra were measured by a LabRAM HV Evolution (HORIBA). A 532 nm laser was used with 1% ND filter. The data were accumulated 5 times for 10 sec.

2.5.5   X-ray Diffraction (XRD)

XRD was measured by D8-Advance (Bruker Miller) using Cu Kα as the X-ray source. Glass substrates were used for the measurements.

2.5.6   Photoluminescence

PL was measured by iBeam smart (TOPTICA PHOTONICS). The laser excitation wavelength was 375 nm with 10 mW output power. The beam diameter was 1.3 mm.

2.5.7   Luminance Image

Device operation image was taken by ECLIPSE LV150NL (Nikon) with digital camera for microscope HK5CCD-S (KOPTIC).

Chapter 3

Degradation Mechanism Analysis on Inverted Perovskite Solar Cells via Restoration of the Ag Electrode

3.1 Introduction

Organic-inorganic hybrid perovskite solar cells have been highlighted as strong candidates for the next generation energy sources required to meet the continuously increasing demand for sustainable energy. The power conversion efficiencies (PCEs) of PSCs have exceeded 20% with outstanding characteristics, such as high absorption coefficients, long exciton diffusion lengths, and easy cell fabrication processes.[24-28] Although researchers have devoted considerable efforts to the development of cost-

effective high-efficiency PSCs, the lifetime of PSCs is still under debate. The natural weak bonding characteristics of methyl ammonium (MA) and iodine make the perovskite film unstable with respect to humidity, with methyl ammonium lead triiodide (MAPbI$_3$) PSCs suffering photovoltaic degradation under ambient air containing a standard level of humidity.[29-31] Even under inert conditions without humidity, MAPbI$_3$ still shows a drop in efficiency.[32] The efficiency drop under inert conditions implies that degradation may originate not only in the perovskite layer but also in the adjacent buffer passivation layers.

An inverted PSC represents a p-i-n-type structure, where the perovskite layer is deposited on the p-type hole transporting layer (HTL), and the n-type electron transporting layer (ETL) is deposited on top of the perovskite layer. There is a wide range of options for the HTL, such as poly(3,4-ethylenedioxythiophene)-poly(styrenesulfonate) (PEDOT:PSS), poly[bis(4-phenyl)(2,4,6-trimethylphenyl)amine] (PTAA), or nickel oxide (NiO). Each HTL has its own specific electrochemical characteristics used for enhancing the hole transport rate or the grain size in the perovskite film or extending the lifetime of the solar cells.[33-35] However, few materials can be used for the ETL because of the requirements for the solvent properties not to damage the perovskite layer and to ensure the proper energy level alignment with the perovskite layer. PCBM is the most widely used ETL material in inverted PSCs because it satisfies these electrochemical conditions. Fullerenes exhibit strong interactions with the halide group elements.[36-38] Therefore, the perovskite layer shows an innate electrochemical reaction with the PCBM layer, forming ETL-related lifetime trend variations or unique charge transport

30

characteristics. Thus, quantitative investigations of lifetime-dependent electrochemical properties of the perovskite/PCBM and PCBM/electrode interfaces are essential for obtaining an understanding of the basic degradation mechanism of inverted PSCs.

In this work, we conducted an in-depth investigation of the degradation mechanism under long-term stability (over 1000 hours) of inverted MAPbI$_3$ PSCs. We focused on the investigation of the interfacial degradation of the devices, especially the interface between PCBM and the Ag electrode. Through a restoration of the Ag electrode by electrode peel off and re-evaporation, we observed straightforward evidence of PSC degradation and a unique trend of lifetime-dependent photovoltaic parameter variation.
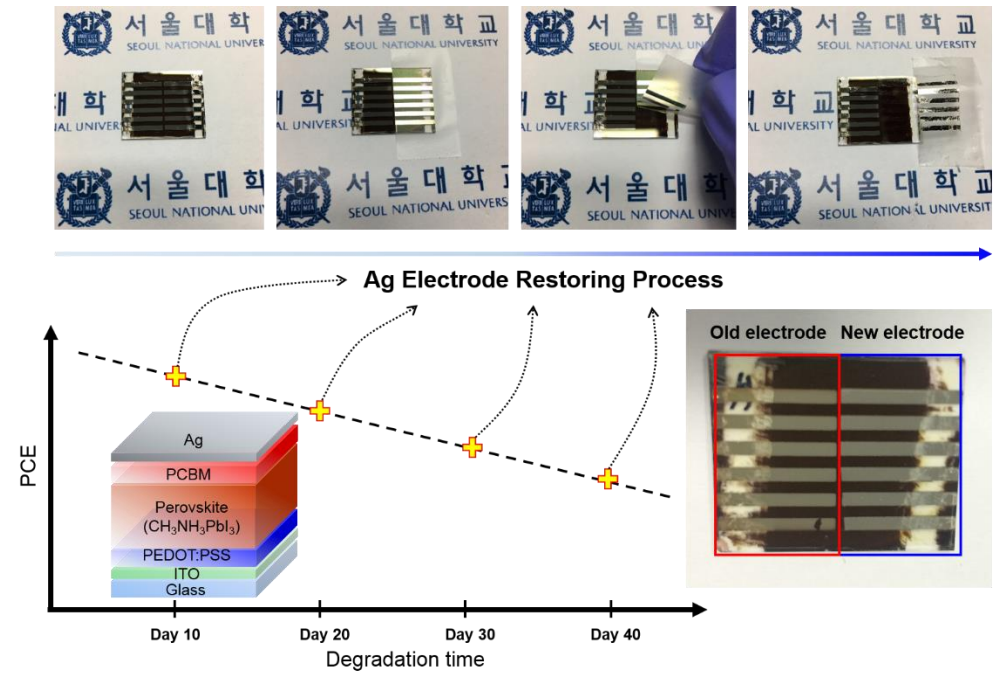
Figure 3.1 Experimental process of the Ag electrode restoration and the device structure. Yellow crosses represent the Ag electrode exchange points. On one substrate, only half of the Ag electrode was peeled off and re-evaporated, as marked by the red and blue boxes.

3.2   Decay Trends of Photovoltaic Parameters

A simple structure of inverted PSCs was used to minimize the additional loss mechanism from additional layers. The p-i-n inverted MAPbI$_3$ PSCs consist of indium tin oxide (ITO)/PEDOT:PSS/MAPbI$_3$/PCBM/Ag. Figure 3.1 shows the experimental process of the Ag electrode restoration. Photovoltaic decay was measured for over 30 devices over 1000 hours. At each electrode restoration (days 10, 20, 30, and 40), 8 devices underwent the process of Ag electrode peel off and re-evaporation. The method of Ag electrode restoration is as follows: *(1) Scotch tape was attached on top of the Ag electrode; (2) pressure was applied to the surface; (3) Scotch tape was removed with the peeled-off Ag electrode; (4) a new Ag electrode was evaporated on the same area where the previous Ag electrode was detached*. Physical damage to PCBM or the perovskite layer during the Ag electrode restoration was not observed (Figure 3.2). On one substrate, only half of the PSC devices went through the process of Ag electrode peel off and re-evaporation, and the other half of the substrate remained unchanged. Thus, a reliable comparison was performed to obtain all electrode restoration comparison data shown in the last part of this paper.
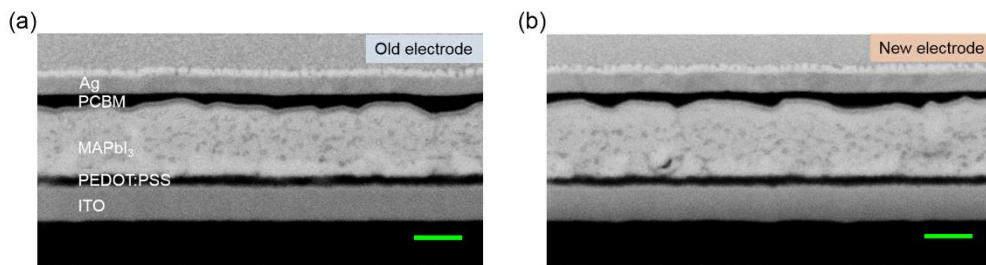
Figure 3.2 Cross-sectional SEM image of the day 10 a) old electrode and b) new electrode devices. Green scale bar represents a length of 200 nm.
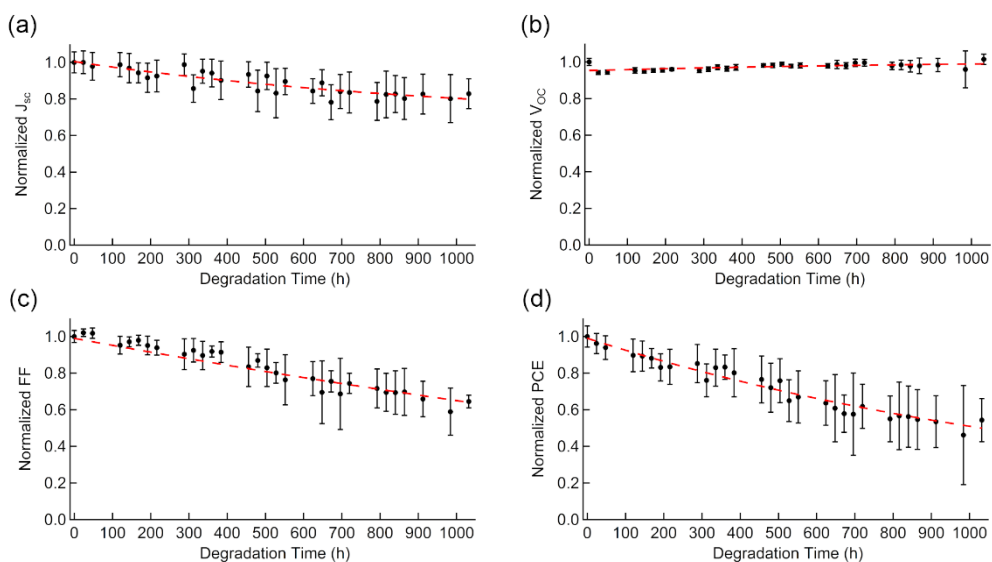
Figure 3.3 Normalized long-term degradation trends of a) J_{SC}, b) V_{OC}, c) FF, and d) PCE. Each parameter is the result of average values over 30 devices.
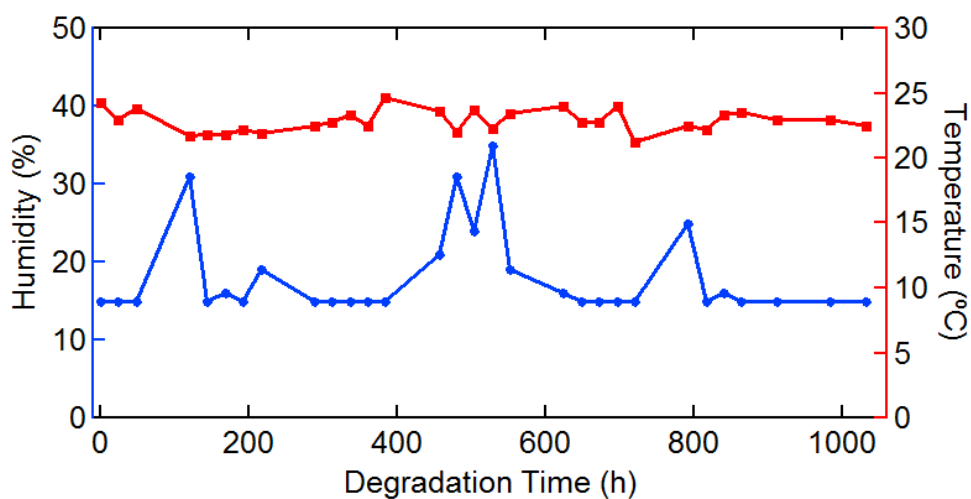
Figure 3.4 Device storage conditions.

The long-term degradation trends of the photovoltaic parameters are shown in Figure 3.3. The device storage conditions (temperature, humidity) are shown in Figure 3.4. The short circuit current density (J_{SC}) and fill factor (FF) showed continuously decreasing tendencies. Interestingly, the open-circuit voltage (V_{OC}) showed a different trend. For the first 10 days of degradation, the V_{OC} decreased by approximately 50 mV. However, it then started to increase and recovered its original value at approximately day 20 (480 h). The V_{OC} even showed a higher value over 1000 hours of degradation.
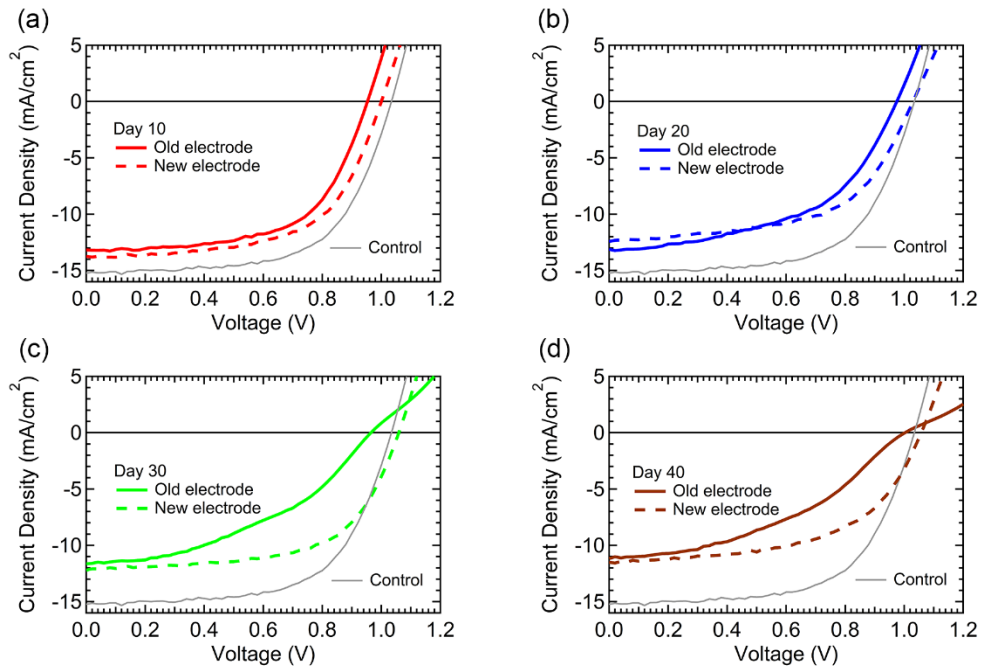
Figure 3.5 Photovoltaic performance of the a) day 10, b) day 20, c) day 30, and d) day 40 Ag electrode restoration points. Each graph represents the photovoltaic performance of the old electrode (solid line), new electrode (dashed line), and control devices (gray solid line).

The photovoltaic performance of each of the electrode restoration points is shown in Figure 3.5. Table 3.1 summarizes the average values of each photovoltaic parameter as a function of the degradation time and electrode restoration process points. The *Old electrode* for each electrode restoration point represents "before Ag electrode peel off" and *New electrode* represents "after Ag electrode peel off and re-evaporation". From day 10 to day 40, each process point showed a similar photovoltaic parameter change. New electrode J_{SC} was slightly decreased or maintained its old value. New electrode V_{OC} was higher by ~50 mV than the value for the old electrode. The new electrode FF showed an enhancement compared to its old value. Due to these changes, the degraded PCE was recovered and saturated by the Ag electrode restoration process. The degradation trend in the inverted PSCs and photovoltaic parameter variation by the Ag electrode restoration process indicates the following four points: (1) a decrease in the J_{SC} value by the Ag electrode restoration process; (2) an increase in the V_{OC} value by the Ag electrode restoration process; (3) a long-term down and up V_{OC} degradation tendency; (4) an increase of the FF value by the Ag electrode restoration process.

Table 3.1. Dependence of the photovoltaic parameters on the degradation time and electrode restoration process.

	Control	Day 10 Old	Day 10 New	Day 20 Old	Day 20 New	Day 30 Old	Day 30 New	Day 40 Old	Day 40 New
J_{SC} (mA/cm²)	15.8	13.7	13.7	13.7	12.3	12.8	11.8	12.4	12.2
V_{OC} (V)	0.98	0.92	0.96	0.97	1.02	0.99	1.04	1.02	1.06
FF (%)	67.7	56.2	62.2	51.0	57.7	44.7	60.0	41.7	56.0
PCE (%)	10.4	7.0	8.2	6.7	7.3	5.7	7.3	5.3	7.3

Average of 4 devices for electrode exchange; Forward scan based

3.3   Direct Evidence of MAPbI3 Solar Cell Degradation

The cross-sectional SEM images taken before and after the Ag electrode peel off and re-evaporation (Figure 3.2) confirmed that the Ag electrode restoration process did not give rise to any physical damage or distortion. Thus, the electrochemical degradation of the Ag/PCBM interfacial layer was mainly considered as the origin of the variation of the photovoltaic parameters. Figure 3.6(a)~(c) shows the depth profiles of the time-of-flight secondary ion mass spectrometry (TOF-SIMS) of the control, old electrode, and new electrode devices. TOF-SIMS is a very sensitive tool for investigating the distribution of selective ions. Each PSC constituent layer was assigned to the representative ions. The Ag^- ion (red line) indicates the Ag electrode,
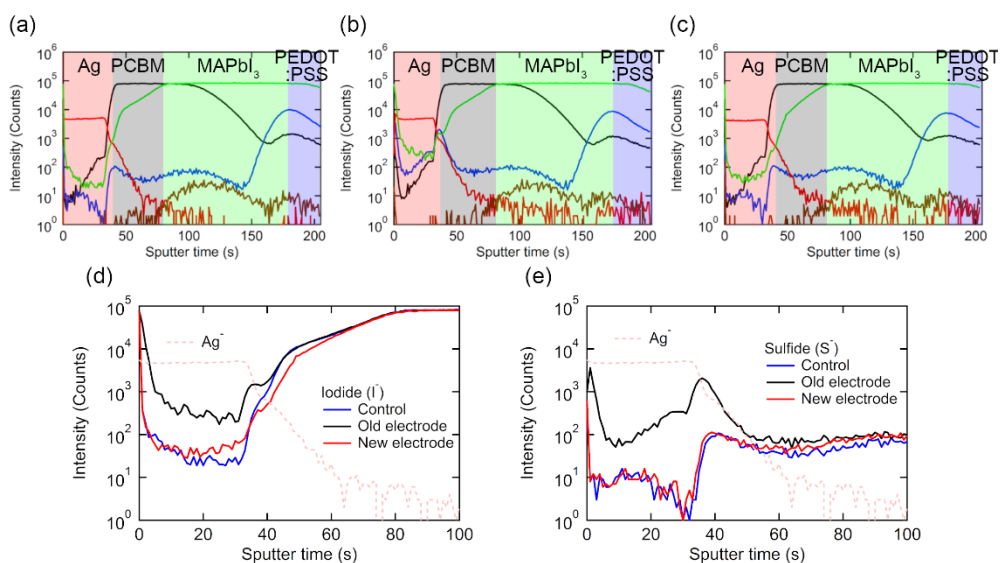
Figure 3.6 TOF-SIMS profiles of the a) control device, b) day 40 old electrode device, and c) day 40 new electrode device. Magnified TOF-SIMS profiles of d) iodide and e) sulfide.

the C$^-$ ion (black line) indicates PCBM, the I$^-$ (green line) and Pb$^-$ (brown line) ions represent the perovskite, and the S$^-$ ion (blue line) indicates PEDOT:PSS. The distribution of each of the elements constructs an observable layer boundary of the PSC. The most prominent findings obtained from the TOF-SIMS experiments are the change in the distribution of the I$^-$ and S$^-$ ions by the Ag electrode peel off and re-evaporation. Figure 3.6(d) and (e) shows a comparison of the graphs of the I$^-$ and S$^-$ ion distributions depending on the Ag electrode restoration process. The I$^-$ and S$^-$ ion levels of the degraded devices (black line) in the Ag layer (sputter time, 0 ~ 40 s) were one order higher than those of the control devices (blue line). The higher I$^-$ and S$^-$ ion levels in the Ag layer clearly show that the I$^-$ ions diffused from the MAPbI$_3$ layer and the S$^-$ ions diffused from the PEDOT:PSS layer. Because the diffusion of I$^-$ and S$^-$ ions could be interpreted as a form of byproduct from the decomposition of the MAPbI$_3$ land PEDOT:PSS layers, the diffused I$^-$ ions and S$^-$ ions may be direct evidence for our inverted MAPbI$_3$ PSC degradation.[39-42] I$^-$ ions and S$^-$ ions accumulated under the Ag layer (sputter time, 40 s). After the Ag electrode restoration process (red line), the I$^-$ and S$^-$ ion levels in the Ag layer decreased to their original levels. Additionally, the accumulated I$^-$ and S$^-$ ions were removed by the Ag electrode peel off. The elimination of ion states induced a PCE recovery for all the Ag electrode restoration points, as shown in Figure 3.5 and Table 3.1. Thus, the removal of diffused and accumulated defect states may boost the photovoltaic characteristics, resulting in increased V_{OC} and FF but decreased J_{SC}.

3.4   Temperature Analysis

In our perovskite experiments, we employed a temperature range from 200 K to 300 K. Ziffer et al. reported that, for temperatures under 200 K, the exciton to free charge generation was found to be below 30%, suppressing the photogenerated charge extraction to the electrodes.[43] Low-temperature photovoltaic performance data (175 K to 300 K) are presented in Figure 3.7.
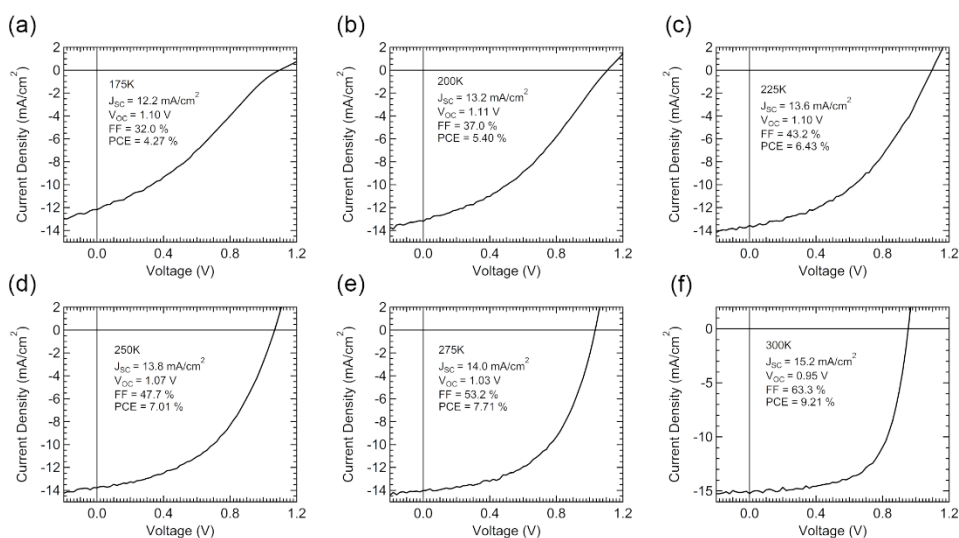
Figure 3.7 Dependence of the photovoltaic performance on temperature: a) 175 K, b) 200 K, c) 225 K, d) 250 K, e) 275 K, and f) 300K. Scan direction is from the short circuit to the open circuit (forward scan).

3.4.1 Activation Energy by Restoring the Ag Electrode

The trapping nature of the carrier dynamics, and especially its influence on J_{SC} and FF, shows an Arrhenius relation between J_{SC} and the temperature (Equation 3.1).

$$J_{SC}(T, P_{light}) = J_0(P_{light}) \cdot \exp(-\frac{\Delta}{K_B T}) \qquad (3.1)$$

Here, T is the temperature, P_{light} is the light intensity, J_0 is the pre-exponential factor determined by photogeneration, recombination, and transport of carriers, K_B is the Boltzmann constant, and Δ is the activation energy. The activation energy is denoted as the energetic depth of the trap states indicating the energy required for the photogenerated charge carriers to overcome the shallow trap states.[44] By taking the natural log of both sides of Equation 3.1, the J_{SC}-temperature graph was plotted for different light intensities, as shown in Figure 3.8.
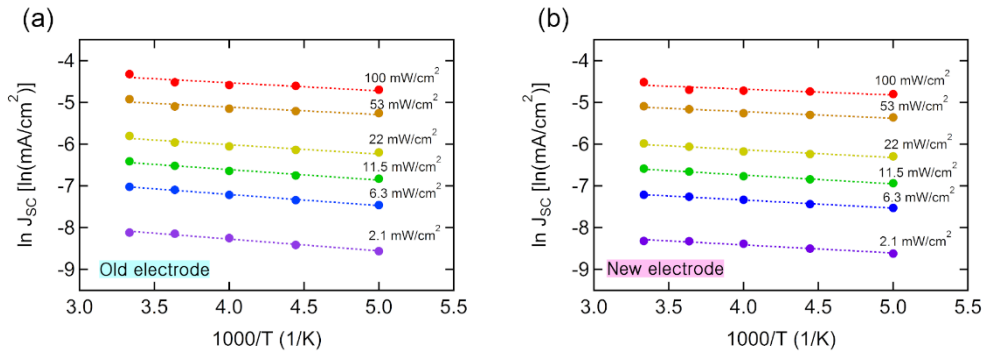
Figure 3.8 Temperature dependence of the J_{SC} by various light intensities for the day 30 a) old electrode and b) new electrode devices. Dashed lines are the linear fitting slopes for the activation energy.
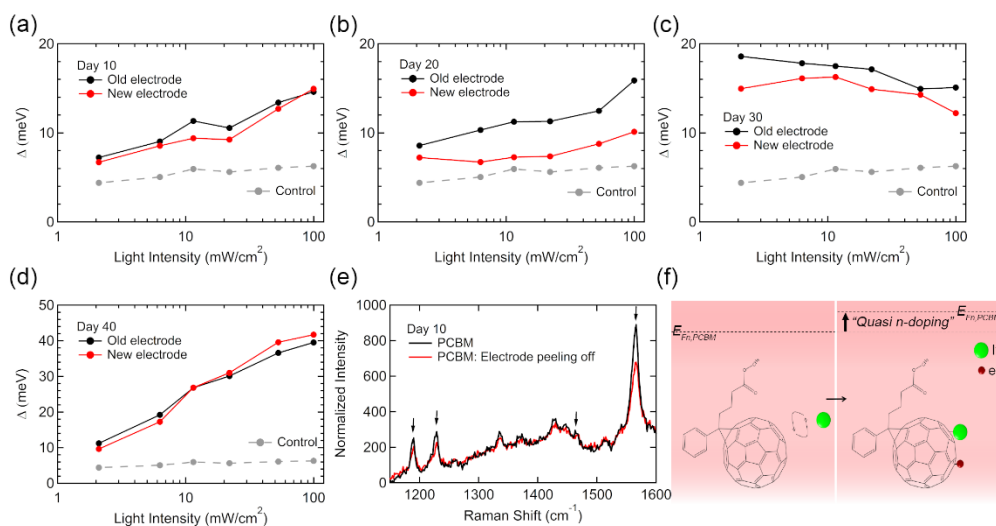
Figure 3.9 Light-intensity-dependent activation energy variation of the a) day 10, b) day 20, c) day 30, and d) day 40 Ag electrode restoration points. Gray dashed lines represent the light-intensity-dependent activation energies of the control device. e) Raman spectra of the day 10 PCBM film (black line) and PCBM film beneath the Ag electrode (red line). f) PCBM-halide interaction process. PCBM-halide radical induces quasi n-doping of PCBM.

Each light-intensity-dependent slope of the J_{SC}-temperature graph provides the activation energy $\varDelta$. Figure 3.9(a)~(d) shows the light-intensity-dependent activation energy for each electrode restoration point. For all the electrode restoration points, the activation energy of new electrode device (red lines) decreased from the degraded values of the old electrode device (black line). Thus, the elimination of the diffused and accumulated defect states by the electrode peel off has a direct influence on the reduction of electronic trap states, resulting in a recovered PCE, especially, FF. While the decreased activation energy may enhance charge extraction by the passivation of trap states, J_{SC} after the electrode restoration process showed slightly decreased values. Xu et al. reported that it is easy for the I^- ions to interact strongly with PCBM. The bonding of PCBM to the halides is thermodynamically favored. The PCBM-halide interaction suppresses the trap states (Pb-I antisite) and enables electron/hole transfer.[38] A PCBM-halide radical was created by the PCBM-I^- interaction, as shown in Figure 3.9(f). Because the PCBM-halide radical is the product of the electron-transfer process, the negatively charged PCBM showed a quasi n-doping effect that gave rise to an increased effective PCBM Fermi level ($E_{Fn,PCBM}$). Thus, the quasi n-doping effect was speculated to enhance charge transport by increasing the electronic level and enabling electron transfer. The removal of accumulated I^- ions by the Ag electrode peel off was confirmed by TOF-SIMS, as shown in Figure 3.6(d). Furthermore, interestingly, the I^- concentration inside the PCBM layer (sputter time 40 s ~ 60 s) was also decreased by the electrode peel off (red line). Hence, we speculated that the decreased concentration of I^- ions inside PCBM decreased the amount of PCBM-halide interaction. The decreased quasi n-doping due to the lower I^- ion concentration suppressed charge transport through the PCBM layer, leading to a decreased J_{SC}. Furthermore, the Raman shift shows the partial bond breaking of the PCBM-halide interaction by the Ag electrode peel off. As

shown in Figure 3.9(e), each of the four peaks marked by arrows are assigned to PCBM. Because the Ag electrode peel off did not lead to a shift in the observed peak positions, the fullerene cage did not dimerize with PCBM. We observed a major drop in the intensity of the 1565 cm^{-1} peak after the Ag electrode peel off. The most intense peak at 1565 cm^{-1} represents the localized vibration of the C5 and C6 fullerene cage rings. The drop in the intensity of the 1565 cm^{-1} peak could be interpreted as a crevice of solubilizing side group attached to the C70 cage or a bond disruption.[45] Because the I^{-} ions preferred to attach to the C70 face rather than to the O face, the detached halide ions may be considered as broken bonds.[38] Thus, the decreased 1565 cm^{-1} Raman peak provides direct evidence for the breaking of the PCBM-halide interaction by the Ag electrode peel off.

3.4.2 V_{OC} Disorder Model by Restoring the Ag Electrode

The data showing the increase in the V_{OC} due to the Ag electrode restoration process are presented in Figure 3.5 and Table 3.1. For all the electrode exchange points, V_{OC} increased by 50 mV. The V_{OC} increase could be related to energetic disorder. [46-49] Structural or chemical features of PCBM, such as random molecular orientations, an amorphous state, or large energetic disorder, immensely affects the V_{OC}. We consider the perovskite layer to have a very low energetic disorder compared to the adjacent organic buffer layers, as the perovskite has high crystallinity with a low trap state density.[47, 50] The distribution of the quasi Fermi level splitting of electrons and holes under illumination plays a crucial role in determining the V_{OC} value of the entire device. The quasi Fermi level splitting of the PCBM layer is also important for determining the V_{OC}. The quasi Fermi level splitting is increased when the available electronic states are occupied by photogenerated carriers. However, the energetic

disorder of PCBM induces additional electronic trap states. Photogenerated carriers tend to settle down to these energetic disorder states, reducing the quasi Fermi level splitting and thus reducing the V_{OC}.
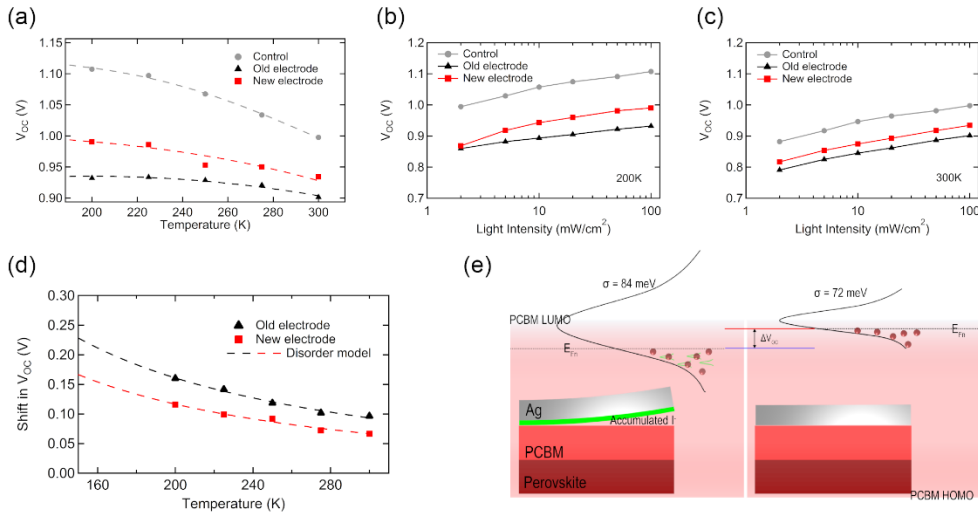
Figure 3.10 a) Temperature dependence of the V_{OC} of the control, old electrode, and new electrode devices of the day 10 Ag electrode restoration point. Light-intensity dependence of the V_{OC} for temperatures of b) 200 K and c) 300 K. d) Temperature dependence of the V_{OC} difference between the control and old electrode devices (black) and the control and new electrode devices (red). The V_{OC} shifts fit the disorder model well. e) Energetic disorder broadening model before and after the Ag electrode restoration process.

To investigate the energetic disorder change of the PCBM layer by the effect of the Ag electrode restoration, the temperature-dependent V_{OC} shift was plotted. The analytical model of the tail states inside the band gap was derived by Blakesley and Neher.[46] These tail states can be described with a Gaussian distribution.[51-52] They found that energetic disorder, σ, decreases the V_{OC} by $\frac{\sigma^2}{2kT}$. Additionally, σ represents the broadening of the energetic disorder described by $\boldsymbol{\sigma = \sqrt{\sigma_{control}^2 - \sigma_x^2}}$, where x = the new electrode or old electrode. Figure 3.10(a) shows the temperature-dependent V_{OC} distribution of the control, old electrode, and new electrode devices. The V_{OC} differences between the control and old electrode or between the control and new electrode increase with a decreasing temperature. Here, before we apply the disorder model, $\boldsymbol{\Delta V_{OC} = \frac{\sigma^2}{2kT}}$, we should check whether the disorder model is applicable to the entire range of light intensity for reliability. Figure 3.10(b) and (c) shows the light-intensity-dependent V_{OC} graphs for 200 K and 300 K, respectively. The V_{OC} differences between the control and old electrode and between the control and new electrode at different light intensities show steady values for both temperatures. Therefore, we used the average value of the V_{OC} difference at a given light intensity for Figure 3.10(d). Using the disorder model obtained from the average V_{OC} shift for each temperature, the energetic disorder broadening value σ was determined as $\boldsymbol{\sigma_{Old\ electrode} = 84\ meV, \sigma_{New\ electrode} = 72\ meV}$. The energetic disorder value after the Ag electrode restoration ($\boldsymbol{\sigma_{New\ electrode}}$) has been reported in pure PCBM devices by disordered hopping transport models, confirming that our electrode restoration process very efficiently eliminates the defect states of the PCBM layer.[53] As a result, the energetic disorder distribution model before and after the Ag electrode restoration process can be described by Figure 3.10(e). The accumulated and diffused I⁻ ions provide additional electronic trap states (green

Gaussian shape), hindering sufficient carrier occupation of electronic states inside the PCBM layer. Thus, an enhanced energetic disorder due to the electrode restoration indicates a larger quasi Fermi level splitting, which leads to a larger V_{OC}.
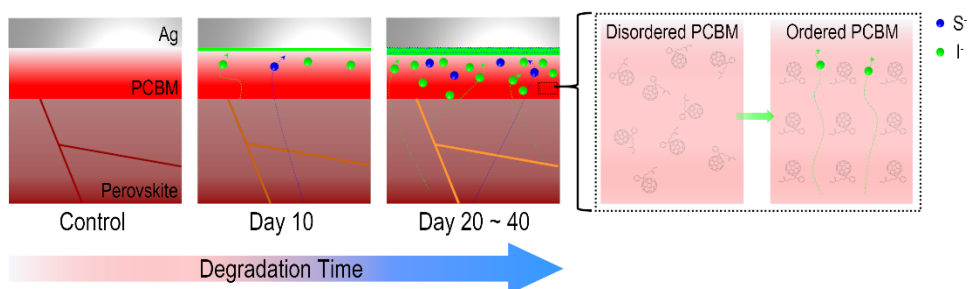
Figure 3.11 Degradation mechanism of inverted MAPbI$_3$ PSCs over the degradation time. Magnified area shows the PCBM ordering process by the PCBM-halide interaction.

3.5   Degradation Mechanism: Structural Ordering of PCBM

As the degradation time increases, V_{OC} decreased for the first 10 days. However, from that point on, the V_{OC} increased slowly and recovered to its original value. The V_{OC} even exceeded its original value after over 1000 hours of degradation, as shown in Figure 3.3(b). As mentioned in the temperature-dependent activation energy section, the I^- ions and PCBM show a very strong interaction. Additionally, the I^- ions favorably attach to the C_{70} face rather than to the O face.[38] We determined that the I^- ions diffused from the $MAPbI_3$ layer and accumulated in the Ag electrode during PSC degradation (Figure 3.6, TOF-SIMS). This can be interpreted as the diffusion of I^- ions having a preferential direction from the perovskite layer to the Ag electrode. The directional diffusion of the I^- ions transforms the randomly oriented PCBM into organized PCBM through the PCBM (C_{70} face) - I^- ion interaction. According to Shao et al., solvent annealing of PCBM provides an ordered PCBM structure, which increases the V_{OC}.[47] Thus, increasing the I^- diffusion with degradation time gives rise to stronger PCBM-I^- interactions, leading to more organized and ordered PCBM. This structurally ordered PCBM induced a V_{OC} increase in our time-dependent PSC degradation, as shown in Figure 3.11. However, the V_{OC} decreased until day 10. This V_{OC} reduction may originate from the degradation of the $MAPbI_3$ film. As shown in Figure 3.5 and Table 3.1, huge burn-in loss of the PCE (33%) was observed for the first 10 days. The J_{SC} and FF decreased by 13% and 17%, respectively. Compared to the other electrode exchange points, the first 10 days of J_{SC} reduction were the worst. The J_{SC} drop is highly related to the light absorber ($MAPbI_3$) degradation. Furthermore, at the day 10 Ag electrode restoration point, we did not observe a J_{SC} drop. As discussed above in the temperature-dependent activation energy section, Ag-PCBM interfacial degradation induced quasi n-doping of PCBM.
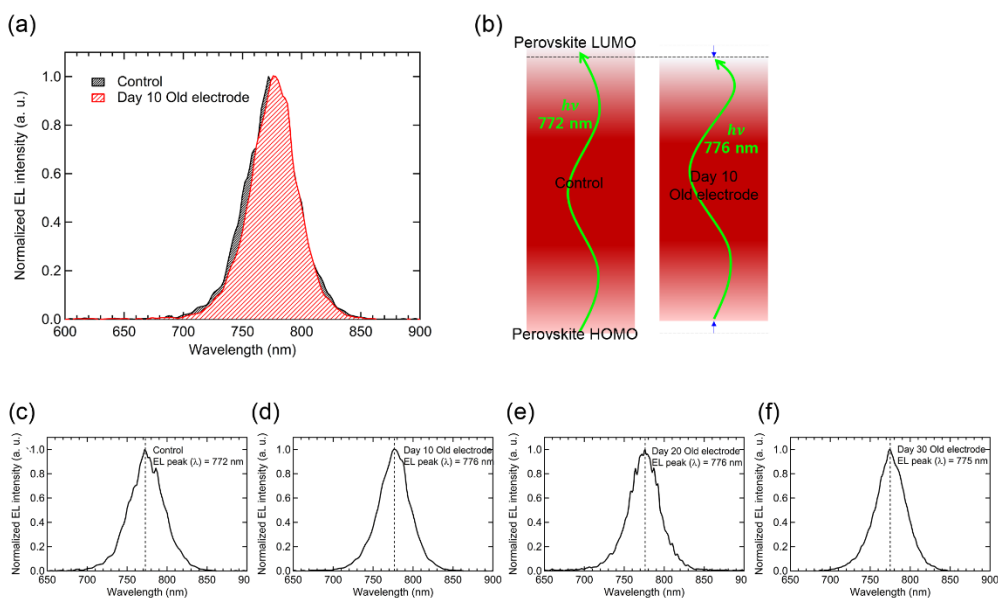
Figure 3.12 a) Normalized EL peak comparison between the control device and the day 10 old electrode device. b) Band-gap shrinkage of the day 10 old electrode device. c) ~ f) Dependence of the normalized EL peak on the degradation time. After the day 10 point, there was no peak shift by degradation.

The Ag electrode restoration process eliminated diffused and accumulated I⁻ ions, which decreased the quasi n-doping J_{SC} reduction. Thus, for the first 10 days of degradation, degradation of the MAPbI$_3$ layer was dominant rather than the PCBM-related interfacial degradation. Figure 3.12 shows the results of electroluminescence (EL) experiments of the control and old electrode devices. The control device emitted 772 nm light, but the day 10 old electrode device emitted 776 nm light. The redshift of the light emission provides direct evidence for the perovskite band-gap shrinkage by degradation. We can suggest a degradation mechanism for the inverted MAPbI$_3$ PSC, as shown in Figure 3.11. For the first 10 days, the degradation of the perovskite layer results in a considerable deterioration of the PCE, inducing a burn-in loss of the

photovoltaic parameters. Here, the recombination process inside the perovskite layer was dominant rather than the interfacial recombination process. After the day 10 Ag electrode restoration point, the perovskite layer continuously degraded with an increased degradation time. More diffused and accumulated I^- and S^- ions created defect recombination states around the Ag/PCBM interface. Thus, interfacial recombination as well as the recombination of the perovskite layer became important. The directional diffusion of the I^- ions interacted with the C_{70} face of PCBM, generating structurally ordered PCBM and continuously increasing the V_{OC}.

3.6   Summary

We studied the degradation mechanism of inverted MAPbI$_3$ PSCs. Ag electrode peel off and re-evaporation enabled us to focus only on the degradation of the interface between the Ag electrode and PCBM layer. The diffusion and accumulation of I$^-$ and S$^-$ ions provided direct evidence of the degradation sources in our PSCs. We demonstrated that diffused I$^-$ ions showed a strong interaction with PCBM that induced quasi n-doping and structural ordering of PCBM. The correlation of the halide-PCBM electrochemical reaction to the variation of the photovoltaic parameters suggested the key mechanism for device operation and degradation. In particular, the V_{OC}-disorder relationship supports the reported studies that showed that the V_{OC} increased as a result of degradation. In addition, we speculate that this key mechanism for inverted PSCs suggests a direction for further improvement of the device stability.

Chapter 4

Degradation Mechanism Analysis on Inverted Perovskite Light-Emitting Diodes

4.1   Introduction

Since the first solid-state perovskite solar cell was reported 2012, research progress of perovskite optoelectronics (solar cells, light-emitting diodes, lasers and thin film transistors) have been developed rapidly.[2, 7, 54-57] High absorption coefficient ($\alpha \sim$ $1.5e^4$ at 550 nm) and long electron-hole diffusion length ($D \sim 100$ nm for $CH_3NH_3PbI_3$) are favorable properties of perovskite which make perovskite solar cells preeminent among competing emerging photovoltaics (organic, dye sensitized, and copper indium

gallium selenide types).[26, 58-59] In 2014, Z. K. Tan et al. reported the first perovskite light-emitting diodes (PeLEDs).[6] High color purity (full width half-maximum (FWHM) of electroluminescence (EL) < 25 nm) and stoichiometric color tunable characteristics are the most advantageous features over competing EL devices (organic and quantum dot).

PeLEDs have issues to be solved as an aspect of film formation and operational stability. At the early stage of PeLED research, PeLEDs exhibited poor EL performance caused by poor perovskite film morphology.[7, 60] Pin-holes were created inside of perovskite film during perovskite crystallization under annealing process. Because pin-holes act as a shunt path between electron transport layer (ETL) and hole transport layer (HTL), leakage current of PeLEDs was increased and the device stability was poor.[3] To enhance the perovskite film condition, anti-solvent pinning process was introduced to PeLED fabrication.[7] The anti-solvent (chlorobenzene, chloroform, toluene, ether) drop during perovskite solution spin-coating process ensures fine pin-hole free perovskite film formation. Based on the advanced perovskite film by anti-solvent, PeLEDs with external quantum efficiency (EQE) over 8% and luminance over 15,000 cd/m2 were reported. However, unlike photovoltaics, full color pattern should be defined inside of pixels for the display application. The anti-solvent pinning process can't be applicable to solution processed patterning method such as ink-jet printing. Thus, alternative perovskite film fabrication method to obtain fine perovskite film quality is required. Furthermore, the driving (turn-on) voltage of PeLEDs is around 3 *V* which implies forward bias voltage over 3 *V* is continuously applied during the device operation. Because ion diffusion from the

52

perovskite film during the operation ($V_{app} < 1.2\ V$) of perovskite solar cells was reported, the ion diffusion of PeLEDs under device operation is strongly speculated.[61-62] The forward bias voltage could accelerate the innate ion diffusion of perovskite film, resulting in rapid degradation of EL performance of PeLEDs.

In this thesis, we fabricated PeLEDs with sequential deposition method for the first time. Sequentially deposited perovskite film shows compact and pin-hole free fine film quality. Sequentially deposited perovskite light-emitting diode (SDPeLED) ensures high performance EL parameters (EQE = 2.02%, luminance = 67,557 cd/m^2). Through an in-depth investigation about before and after SDPeLED operation, we found the direct evidence of SDPeLED degradation. Moreover, we proposed a novel ion diffusion induced degradation mechanism of SDPeLEDs.

4.2   Sequential Deposition of Perovskite Films
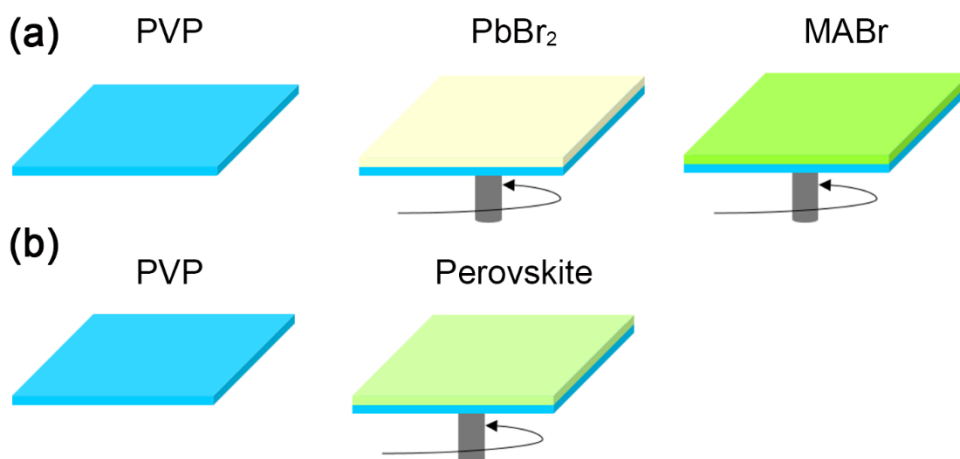
Figure 4.1 Experimental scheme of sequential deposition and one-step deposition. (a) Sequential deposition process of perovskite film. (b) One-step deposition process of perovskite film.

4.2.1   Sequential Deposition Process

Methyl ammonium lead tri-bromide (MAPbBr$_3$) perovskite thin films were fabricated by sequential deposition process. Sequential deposition process and one-step deposition process of perovskite film are shown in Figure 4.1. On top of polyvinylpyrrolidone (PVP) coated substrate, lead bromide (PbBr$_2$) solution was spin coated and annealed. Then, methyl ammonium bromide (MABr) solution was sequentially spin coated and annealed to fabricate compact and pin-hole free perovskite film.
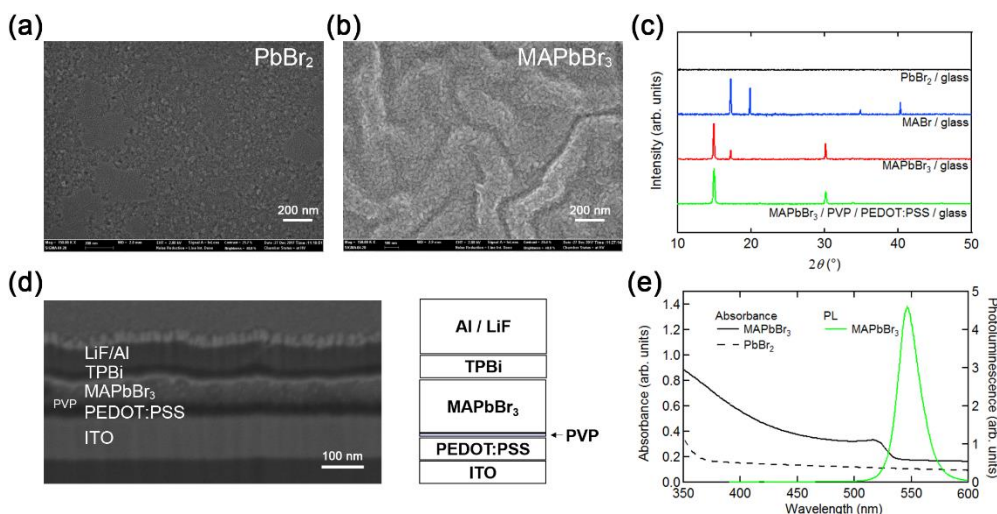
Figure 4.2 Morphology of MAPbBr$_3$ film and film characteristics. Sequentially deposited surface SEM image of (a) PbBr$_2$ and (b) MAPbBr$_3$. (c) XRD of PbBr$_2$ and MAPbBr$_3$ films on top of PEDOT:PSS / PVP coated substrates. (d) Cross sectional SEM image of SDPeLED. (e) Absorbance and photoluminescence of PbBr$_2$ and MAPbBr$_3$. Scale bar is 200 nm in all images.

4.2.2 Morphology and Film Characteristics of Perovskite

Film morphology of sequentially deposited perovskite is shown in Figure 4.2(a) and (b). PbBr$_2$ film shows compact and dense film formation (Figure 4.2(a)) which exhibit amorphous state without any crystal peak in X-ray diffraction (XRD) (Figure 4.2(c) and Figure 4.3). MABr spin-coated MAPbBr$_3$ film shows compact and pin-hole free film formation (Figure 4.2(b)). The grain size of perovskite was less than 50 nm. In the case of PeLEDs, grain size should be less than 100 nm to facilitate efficient radiative bimolecular recombination.[7, 9] Exciton binding energy of perovskite is very low, even excitons thermally generate free charge carriers in room temperature.[63-64]
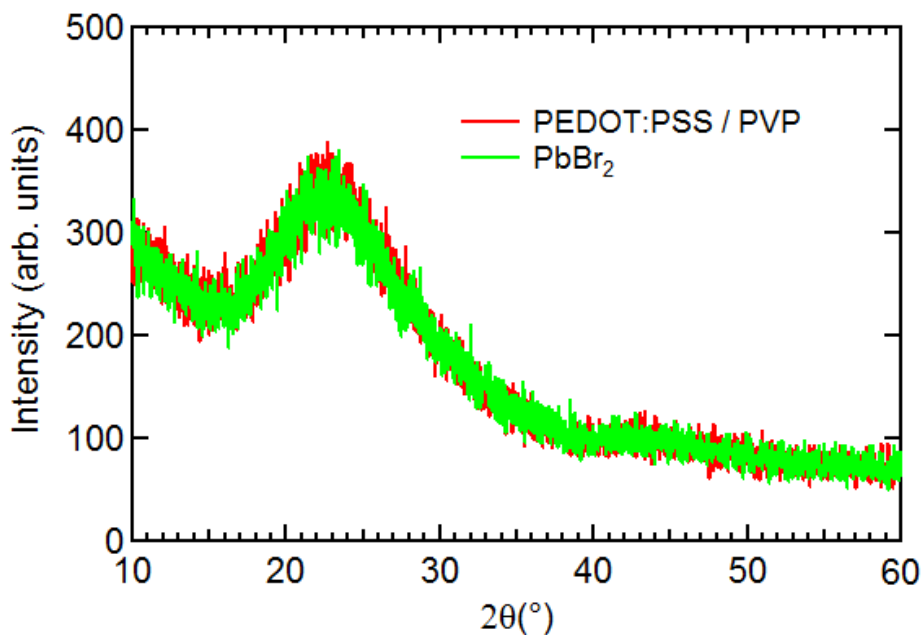
Figure 4.3 XRD of PbBr$_2$. PbBr$_2$ shows amorphous state without any diffraction peak.

Because electron-hole diffusion length of perovskite is about 100 nm, grain size less than 100 nm confines charge carriers effectively. Thus, small grain size of sequentially deposited perovskite film induces high radiative electron-hole binding rate. XRD shows the crystalline property of sequentially deposited perovskite film (Figure 4.2(c)). The diffraction peaks at 14.98°, 30.19°, 33.80° correspond to (001), (002), (021) plane orientation which indicate pure cubic MAPbBr$_3$ phases.[65] We found novel crystalline diffraction peak at 17.29° and 34.90° which are supposed to be the evidence of sequentially deposited perovskite film. Cross sectional scanning electron microscope (SEM) confirms compact and pin-hole free perovskite film (Figure 4.2(d)). Poly(3,4-ethylenedioxythiophene)-poly(styrenesulfonate) (PEDOT:PSS) act as a HTL and very thin (~ 5 nm) PVP layer was inserted to prevent strong optoelectronic quenching from PEDOT:PSS layer.
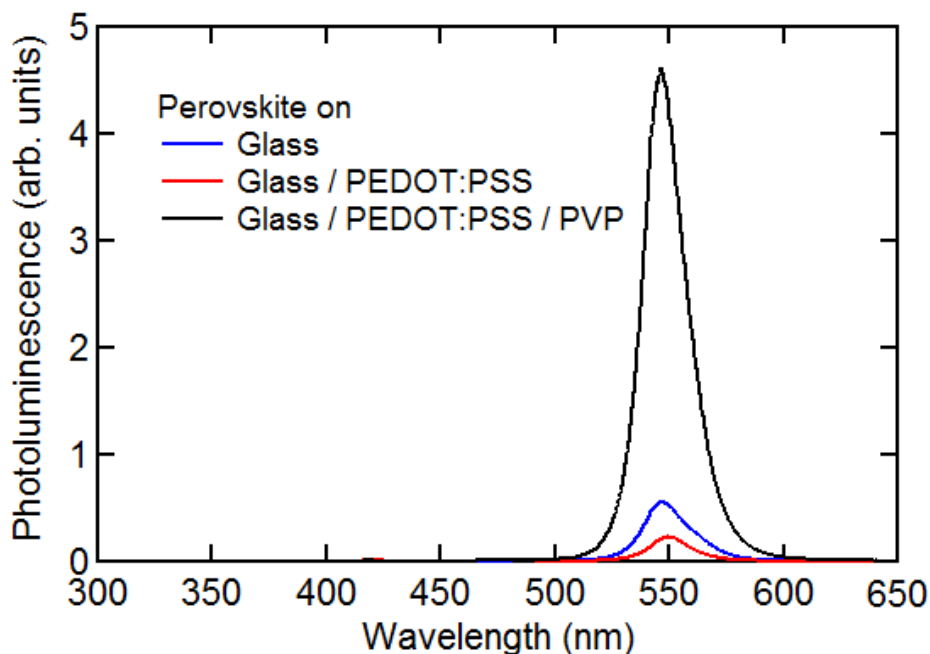
Figure 4.4 PL of sequentially deposited perovskite film on different substrates. PEDOT:PSS act as a strong quenching layer. By inserting PVP, the PL was significantly enhanced.

Bulk MAPbBr$_3$ perovskite layer was used as an emission layer. 2,2',2"-(1,3,5-Benzinetriyl)-tris(1-phenyl-1-H-benzimidazole) (TPBi) act as an ETL. Finally, lithium fluoride (LiF) and Al was evaporated. PbBr$_2$ film has very low absorbance while MAPbBr$_3$ film has absorbance peak at 515 nm with increasing absorbance as photon energy increases. Along with the absorbance peak, sharp photoluminescence (PL) at 546 nm was measured (Figure 4.2(e)). The PL spectra of PVP inserted devices showed much higher intensity than that of without PVP devices (Figure 4.4). Strong non-radiative quenching by PEDOT:PSS was suppressed by inserting PVP layer which promises the enhanced EL performance. We optimized the concentration of each PbBr$_2$ and MABr solutions with respect to the film morphology. The sequentially

deposited perovskite film morphology and absorbance depend on solution concentration are shown in Figure 4.5-4.8.
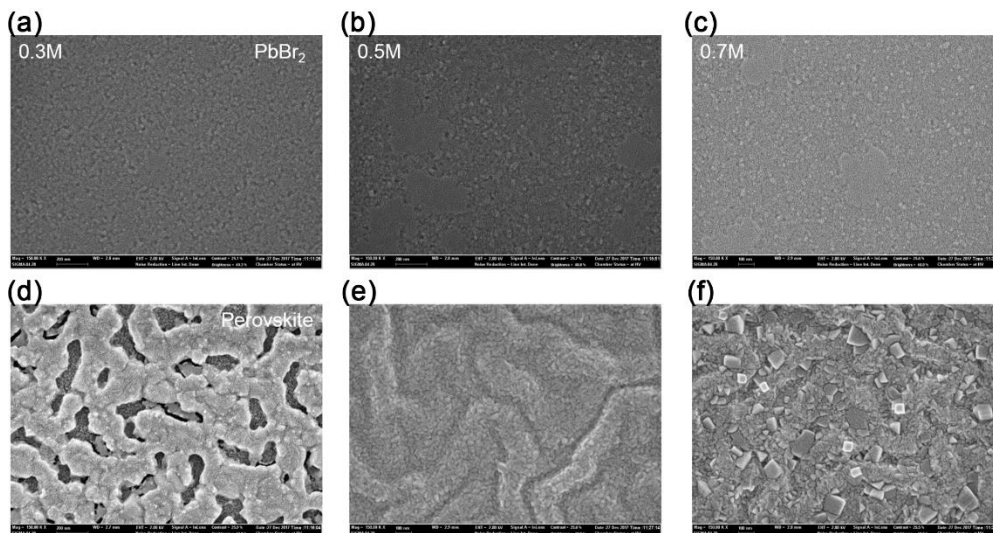
Figure 4.5 Morphology of sequentially deposited perovskite film. (a-c) SEM image of PbBr$_2$ by different concentration (0.3 M ~ 0.7 M). Each PbBr$_2$ film shows compact and pin-hole free state. (d-f) SEM image of perovskite film by sequential deposition of MABr (10 mg/ml). Perovskite film with 0.3 M PbBr$_2$ shows many pin-holes. Perovskite film with 0.7 M PbBr$_2$ shows pin-hole free but rough surface, even large grains were created.
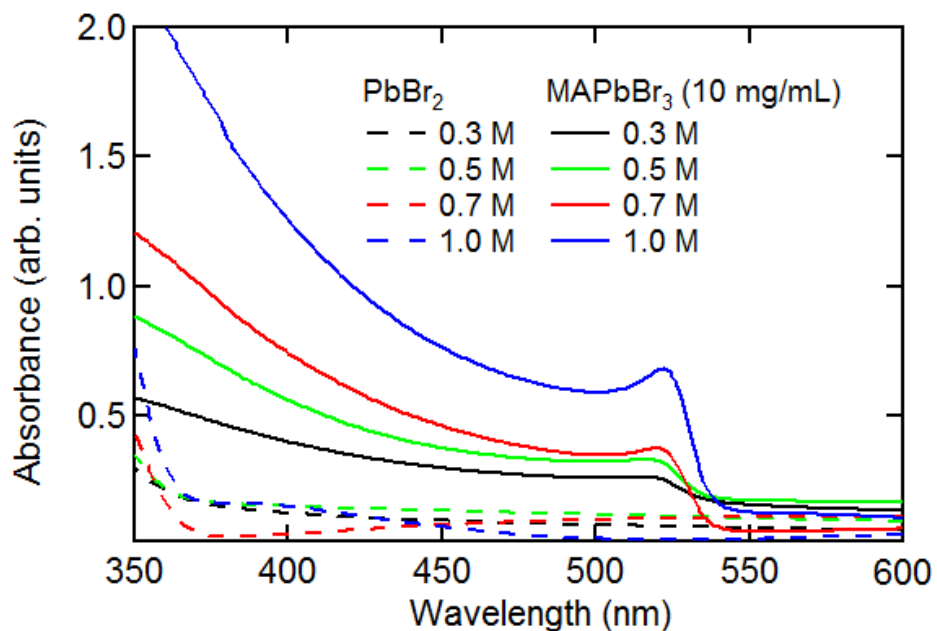
Figure 4.6 Absorbance of different PbBr₂ concentration. PbBr₂ films show bare absorbance in visible wavelength. In case of 0.7 M and 1.0 M PbBr₂ concentration case, absorbance rapidly increases around 350 nm. Perovskite film absorbance shows higher absorbance with higher concentration of PbBr₂. We speculate that the thickness of perovskite is determined by the concentration of PbBr₂.
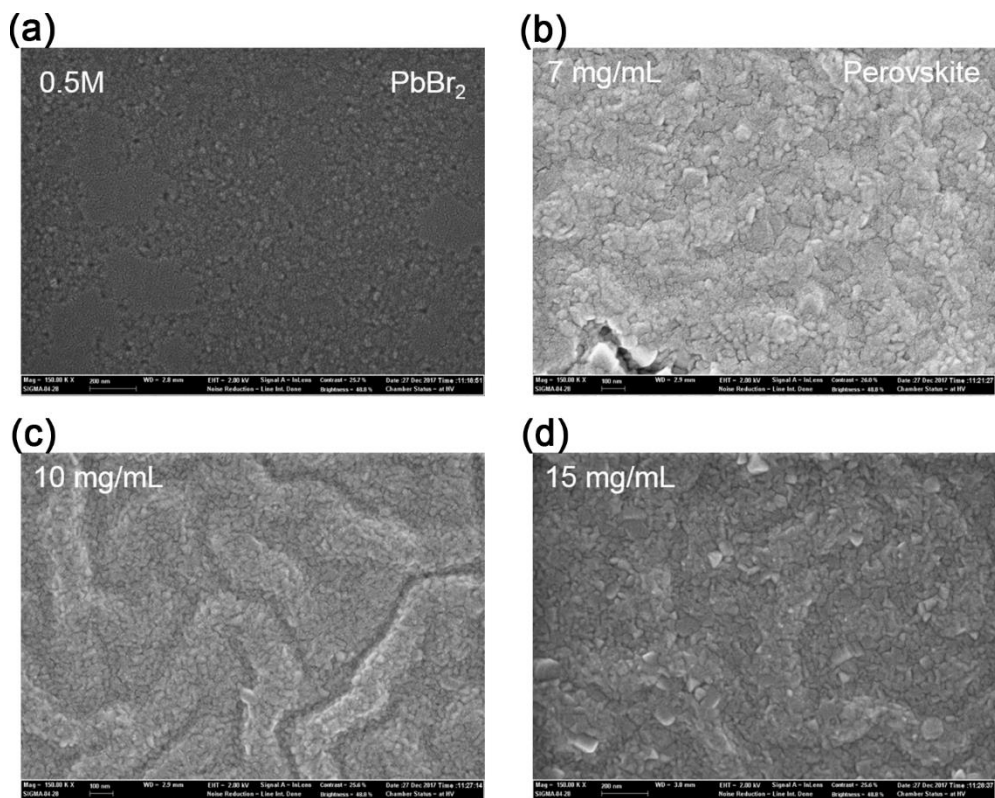
Figure 4.7 Morphology of sequentially deposited perovskite film. Based on the 0.5 M $PbBr_2$ concentration, perovskite film was formed by different concentration of MABr. 7 mg/ml of MABr perovskite film partially shows unreacted area between $PbBr_2$ and MABr. 15 mg/ml of MABr perovskite film shows some over reacted area between $PbBr_2$ and MABr. The grain size was larger than 10 mg/ml case.
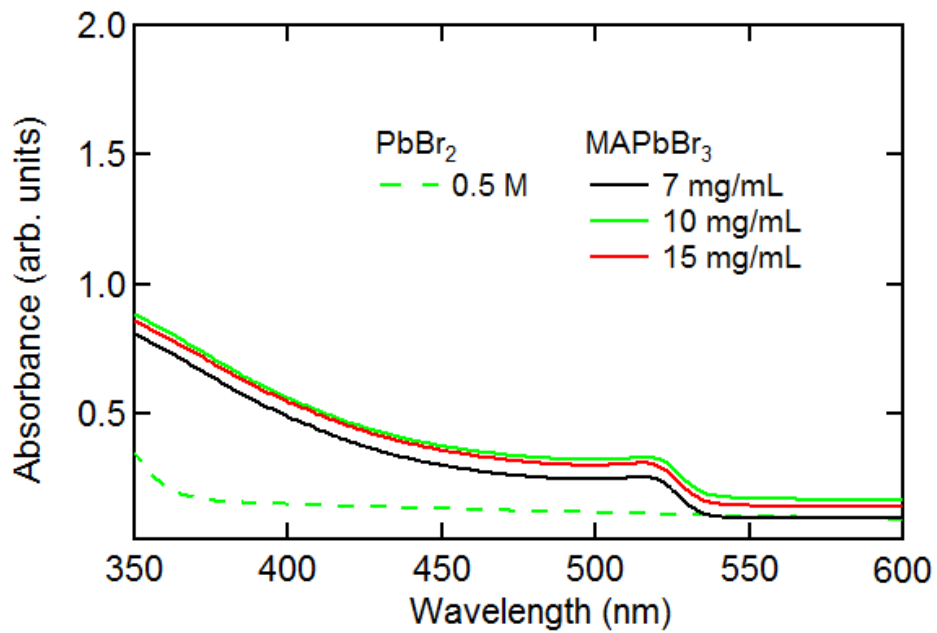
Figure 4.8 Absorbance of different MABr concentration. Absorbance barely changes by different MABr concentration.

4.3 Electroluminescence of Perovskite Light-Emitting Diodes

4.3.1 PbBr₂ Concentration Dependent Electroluminescence Characteristics

The EL performance of SDPeLED depend on $PbBr_2$ concentration is shown in Figure 4.9. Current density – voltage plot is shown in Figure 4.9(a). The luminance is continuously increased as current density increases (Figure 4.9(d)). The maximum luminance was 45587, 67557, 7433, and 112 cd/m² for each $PbBr_2$ concentration. The SDPeLED shows maximum current efficiency (CE) 6.02, 8.94, 6.94, and 0.04 cd/A and maximum EQE 1.40, 2.02, 1.57, 0.01% for each $PbBr_2$ concentration (Figure 4.9(b) and (c)). The EL spectrum peak was located at 533 nm and the FWHM of the spectrum was 22 nm (Figure 4.9(e)). The EL performance of SDPeLED depend on $PbBr_2$ concentration is summarized in Table 4.1.
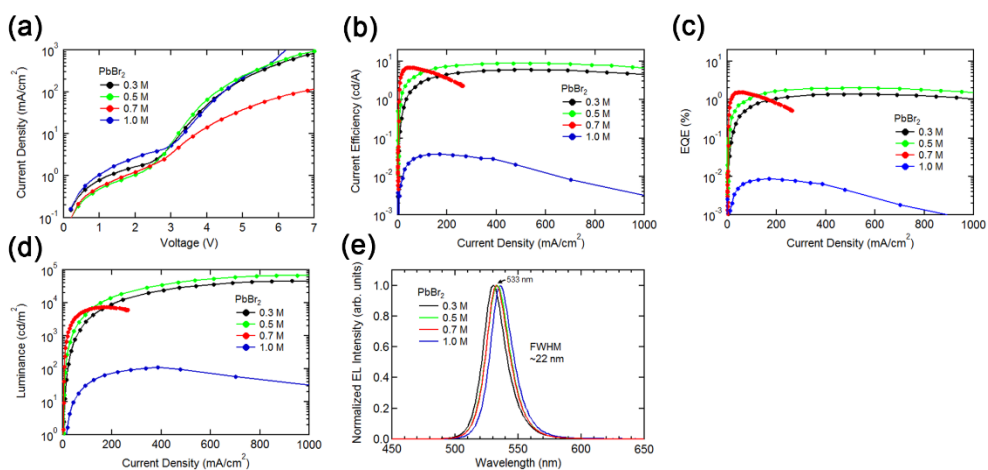
Figure 4.9 EL performance of different concentration of PbBr$_2$. (a) *J-V* curve of SDPeLED with different concentration of PbBr$_2$. (b) CE graph of SDPeLED with respect to current density. (c) EQE graph of SDPeLED with respect to current density. (d) Luminance graph of SDPeLED with respect to current density. (e) EL spectrum of SDPeLED with different concentration of PbBr$_2$. The concentration of MABr was 10 mg/ml.

Table 4.1. Device performance of SDPeLED with different concentration of PbBr$_2$.

PbBr$_2$	Max. CE (cd/A)	Max. EQE (%)	Max. luminance (cd/m^2)	Peak wavelength (nm)
0.3 M	6.02	1.40	45,587	530
0.5 M	8.94	2.02	67,557	533
0.7 M	6.94	1.57	7,433	533
1.0 M	0.04	0.01	112	536

4.3.2 MABr Concentration Dependent Electroluminescence Characteristics

The EL performance of SDPeLED depend on MABr concentration is shown in Figure 4.10. Current density – voltage plot is shown in Figure 4.10(a). The luminance is continuously increased as current density increases (Figure 4.10(d)). The maximum luminance was 531, 67557, and 15858 cd/m^2 for each MABr concentration. The SDPeLED shows maximum current efficiency (CE) 0.05, 8.94, and 1.35 cd/A and maximum EQE 0.01, 2.02, and 0.31% for each MABr concentration (Figure 4.10(b) and (c)). The EL spectrum peak was located at 533 nm and the FWHM of the spectrum was 22 nm (Figure 4.10(e)). The EL performance of SDPeLED depend on MABr concentration is summarized in Table 4.2.
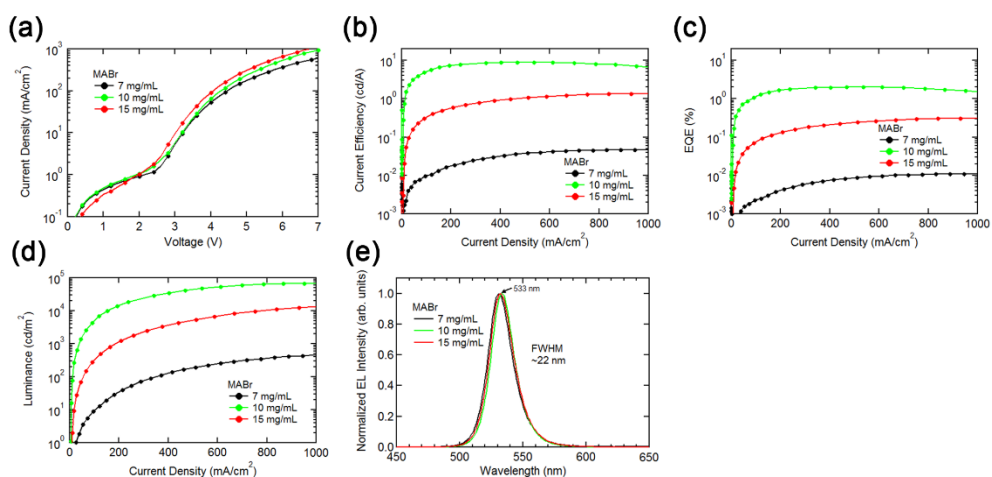
Figure 4.10 EL performance of different concentration of MABr. (a) *J-V* curve of SDPeLED with different concentration of MABr. (b) CE graph of SDPeLED with respect to current density. (c) EQE graph of SDPeLED with respect to current density. (d) Luminance graph of SDPeLED with respect to current density. (e) EL spectrum of SDPeLED with different concentration of MABr. The concentration of $PbBr_2$ was 0.5 M.

Table 4.2. Device performance of SDPeLED with different concentration

MABr	Max. CE (cd/A)	Max. EQE (%)	Max. luminance (cd/m^2)	Peak wavelength (nm)
7 mg/mL	0.05	0.01	531	531
10 mg/mL	8.94	2.02	67,557	533
15 mg/mL	1.35	0.31	15,858	532

4.3.3 PVP Concentration Dependent Electroluminescence Characteristics

The EL performance of SDPeLED depend on PVP concentration is shown in Figure 4.11. Current density – voltage plot is shown in Figure 4.11(a). The luminance is continuously increased as current density increases (Figure 4.11(d)). The maximum luminance was 23, 49057, 15638, and 9532 cd/m^2 for each PVP concentration. The SDPeLED shows maximum current efficiency (CE) 0.004, 7.92, 2.69, and 1.95 cd/A and maximum EQE 0.001, 1.83, 0.65, and 0.46% for each PVP concentration (Figure 4.11(b) and (c)). The EL spectrum peak was located at 531 nm and the FWHM of the spectrum was 22 nm (Figure 4.11(e)). The EL performance of SDPeLED depend on PVP concentration is summarized in Table 4.3.
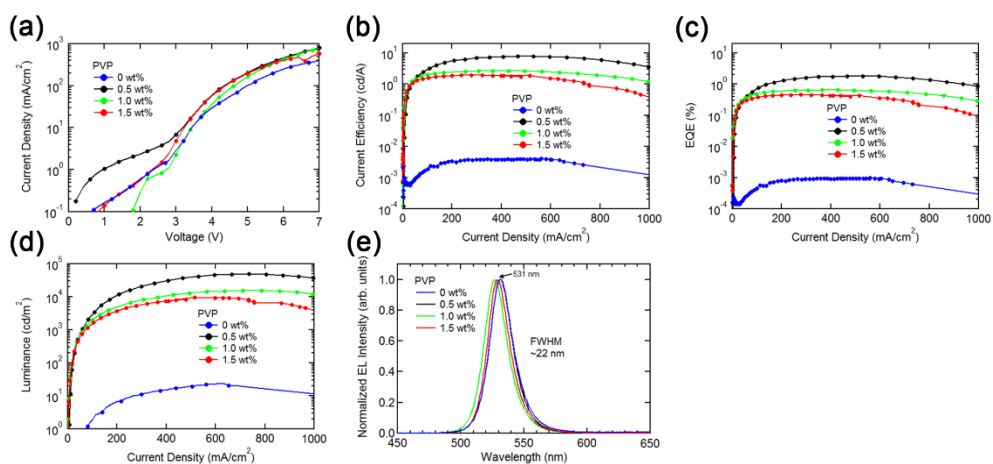
Figure 4.11 EL performance of different concentration of PVP. (a) *J-V* curve of SDPeLED with different concentration of PVP. (b) CE graph of SDPeLED with respect to current density. (c) EQE graph of SDPeLED with respect to current density. (d) Luminance graph of SDPeLED with respect to current density. (e) EL spectrum of SDPeLED with different concentration of PVP. The concentration of $PbBr_2$ and MABr was 0.5 M and 10 mg/ml.

Table 4.3. Device performance of SDPeLED with different concentration of PVP.

PVP	Max. CE (cd/A)	Max. EQE (%)	Max. luminance (cd/m^2)	Peak wavelength (nm)
0 wt%	0.004	0.001	23	531
0.5 wt%	7.92	1.83	49,057	531
1.0 wt%	2.69	0.65	15,638	527
1.5 wt%	1.95	0.46	9,532	529

67

4.3.4 Perovskite Film Annealing Temperature Dependent Electroluminescence Characteristics

The EL performance of SDPeLED depend on perovskite film annealing temperature is shown in Figure 4.12. Current density – voltage plot is shown in Figure 4.12(a). The luminance is continuously increased as current density increases (Figure 4.12(d)). The maximum luminance was 21048, 25708, 2215, and 484 cd/m^2 for each perovskite film annealing temperature. The SDPeLED shows maximum current efficiency (CE) 3.48, 4.43, 0.31, and 0.05 cd/A and maximum EQE 0.82, 1.01, 0.07, and 0.01% for each perovskite film annealing temperature (Figure 4.12(b) and (c)). The EL spectrum peak was located at 532 nm and the FWHM of the spectrum was 22 nm (Figure 4.12(e)). The EL performance of SDPeLED depend on perovskite film annealing temperature is summarized in Table 4.4.
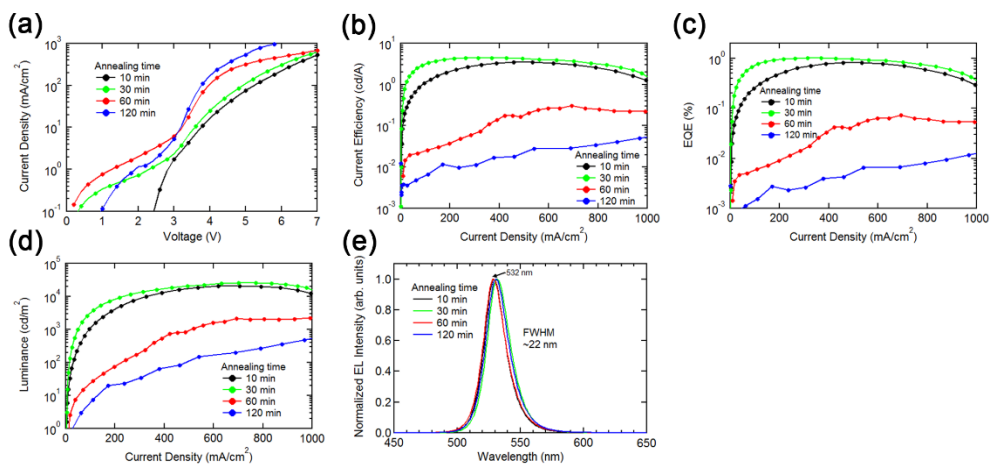
Figure 4.12 EL performance of different annealing time of perovskite film. (a) *J-V* curve of SDPeLED with different annealing time of perovskite film. Annealing temperature was 100℃. (b) CE graph of SDPeLED with respect to current density. (c) EQE graph of SDPeLED with respect to current density. (d) Luminance graph of SDPeLED with respect to current density. (e) EL spectrum of SDPeLED with different annealing time of perovskite film. The concentration of $PbBr_2$ and MABr was 0.5 M and 10 mg/ml.

Table 4.4. Device performance of SDPeLED with different annealing time of perovskite film.

Annealing Time	Max. CE (cd/A)	Max. EQE (%)	Max. luminance (cd/m^2)	Peak wavelength (nm)
10min	3.48	0.82	21,048	529
30min	4.43	1.01	25,708	532
60min	0.31	0.07	2,215	529
120min	0.05	0.01	484	531

4.3.5 Electroluminescence of Optimized Perovskite Light-Emitting Diodes

The EL performance of SDPeLED comparison with one-step deposition perovskite light-emitting diode (ODPeLED) is shown in Figure 4.13. Current density – voltage plot of SDPeLED and ODPeLED is shown in Figure 4.13(a). The luminance of the SDPeLED is continuously increased as current density increases (Figure 4.13(b)). The maximum luminance of SDPeLED was 67,557 cd/m^2. The SDPeLED shows efficient EL performance with maximum current efficiency (CE) 8.94 cd/A and maximum EQE 2.02% (Figure 4.13(c)). Moreover, the efficiency roll-off from maximum efficiency point (500 mA/cm^2) to 1000 mA/cm^2 was very low. Figure 4.13(d) is the operation image of SDPeLED under 100 mA/cm^2 current bias. The EL spectrum peak was located at 533 nm and the FWHM of the spectrum was 22 nm (Figure 4.13(e)). The EL performance of SDPeLED and ODPeLED is summarized in Table 4.5.
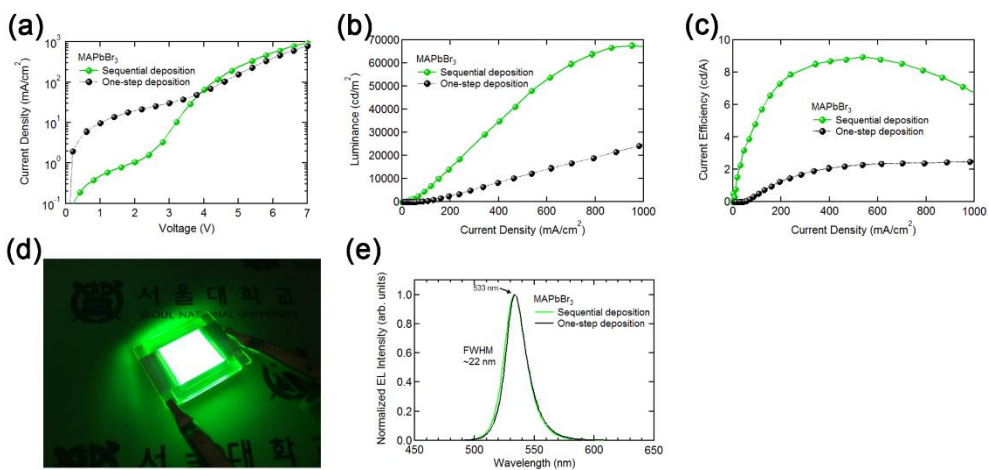
Figure 4.13 EL performance of SDPeLED and ODPeLED. (a) J-V curve of SDPeLED and ODPeLED. (b-c) Luminance and CE graph of SDPeLED and ODPeLED with respect to current density. (d) Operation image of large area (1 cm2) SDPeLED. (e) EL spectrum of SDPeLED and ODPeLED.

Table 4.5. Device performance of SDPeLED and ODPeLED.

MAPbBr$_3$	Max. CE (cd/A)	Max. EQE (%)	Max. luminance (cd/m^2)	Peak wavelength (nm)
Sequential PbBr2 (0.5 M) MABr (10 mg/ml)	8.94	2.02	67,557	533
One-step	2.52	0.57	30,151	534

71

4.4   Degradation of Electroluminescence
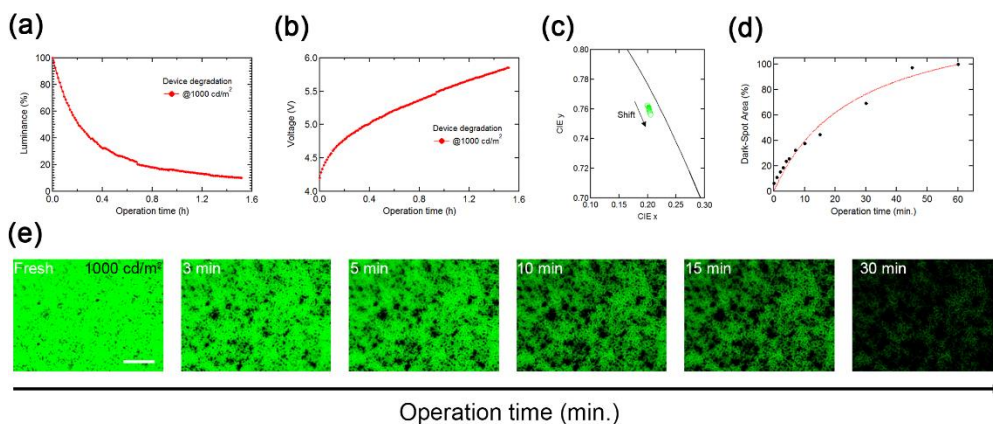
Figure 4.14 Device degradation by continuous current bias. (a) Luminance decay graph of SDPeLED. Initial luminance of device was 1000 cd/m^2. The applied current was and 1.0 mA for each luminance. (b) Applied voltage variant by device degradation. (c) CIE coordinate plot depend on the device operation time. (d) Time dependent dark-spot growth model. Red dotted line represents facilitated diffusion model. (e) Real-time luminance degradation image. Initial luminance of the fresh device was 1000 cd/m^2. Scale bar is 50 μm.

The reports about analysis of PeLED lifetime was inadequate because PeLEDs are very unstable during the device operation.[23, 66-67] We investigated operational device stability of SDPeLED (Figure 4.14). We operated the SDPeLED and measured lifetime in two condition; L_0 (initial luminance) = 1000 cd/m^2. The luminance decay was fast in L_0 = 1000 cd/m^2 condition which exhibited higher applied voltage increase (Figure 4.14(a) and (b)). The half-lifetime (T_{50}) of luminance under 1000 cd/m^2 was 13 min. and applied voltage was increased from 4.2 *V* to 4.8 *V* during device operation. The applied power to device during the device operation continuously increased. This implies that the applied Joule-heat by light-emission per area continuously

increased.[68] Thus, the increase of power load to light-emitting diodes is speculated to accelerate device degradation. Moreover, we found the shift of color coordinate CIE X, Y by device degradation (Figure 4.14(c)). The fresh device exhibited CIE X, Y (0.199, 0.763). After 90% decay of initial luminance (T_{10}), the color coordinate shifted to CIE X, Y (0.205, 0.756). The color coordinate shift can be a critical issue for the future display application because color instability causes balance breaking between red, green, and blue pixels to form white color. The operation images of SDPeLED under 1000 cd/m^2 are shown in Figure 4.14(e) depend on operation time. The large green emission areas gradually turned into the black spots. We found that the increasing time-dependent dark spot area follows the facilitated diffusion model (Figure 4.14(d)). At low operation time stage, the ion concentration is low which exhibit simple linear diffusion model. But, as operation time increases, the diffused ion saturates with limited ion sources. Here, diffused ions are represented as dark spot. We give the equation as:

$$\text{Ion diffusion} = \frac{V_{max}}{1 + K/C} \tag{4.1}$$

where, V_{max} = Saturation constant, K = constant determining speed of saturation, and C = concentration of ion diffusion. From the ion diffusion model, we speculated that the origin of SDPeLED degradation may originate from the ion diffusion by morphological degradation of perovskite film or adjacent layers by constant applied current.

4.5   Direct Evidence of Light-Emitting Diodes

4.5.1   TOF-SIMS Analysis on the Degraded Device
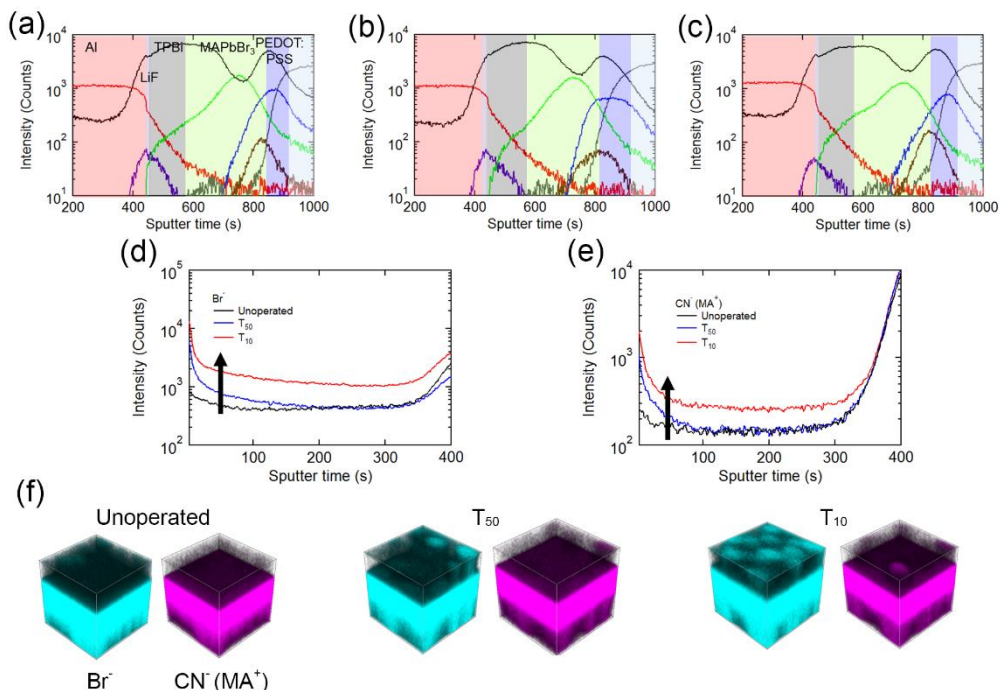
Figure 4.15 Direct evidence of SDPeLED degradation. (a-c) TOF-SIMS depth profiling for unoperated, T_{50}, and T_{10} devices, respectively. Al$^-$ (red), Li$^-$ (purple), CH$^-$ (black), Br_2^- (green), Pb$^-$ (brown), SO_2^- (blue), $In_2O_2^-$ (gray) ions are plotted. (d) Ion distribution of Br$^-$ depend on degradation time. (e) Ion distribution of CN$^-$ (MA$^+$) depend on degradation time. (f) 3D images of Br$^-$ and MA$^+$ ion diffusion from depth profiling of TOF-SIMS. The length of each axis is 70 μm.

To investigate the distributional change of elements with respect to device degradation, the depth profiles of the time-of-flight secondary ion mass spectrometry (TOF-SIMS) were investigated (Figure 4.15). Each layer of SDPeLED has their distinguishable

element to represent. The Al^- ion indicates Al electrode, the Li^- ion indicates LiF, the CH^- ion indicates TPBi and PVP, the Br^- and Pb^- ions represent perovskite, the SO_2^- ion indicates PEDOT:PSS, and $In_2O_2^-$ indicates ITO. Perceivable layer boundary for each SDPeLED constituent layer was constructed (Figure 4.15(a) ~ (c)). Depend on the degradation time, some elements showed distinct distributional change. Figure 4.15(d) and (e) represent TOF-SIMS graph of Br^- ion and CN^- ion. CN^- ion is distinctive ion which represent MA^+ ion in perovskite.[40, 69] As device operation time increases, the ion concentration of Br^- and CN^- inside of Al electrode (sputter time 0 ~ 400 s) increased continuously. Even, the ion concentration of Br^- and CN^- at the surface of Al electrode (sputter time around 0 s) significantly increased. Because Br^- and CN^- (MA^+) ions are the representative ions of the $MAPbBr_3$ layer, Br^- and MA^+ ions are considered to be diffused from the perovskite layer during the device operation. For more detail, the depth profiling of Br^- and CN^- (MA^+) ions was plotted by 3D image (Figure 4.15(f)). The 3D Br^- and CN^- ion distribution clearly shows that Br^- and MA^+ ions were diffused from the perovskite layer to Al electrode during the device operation. Moreover, the diffusion paths of Br^- and MA^+ were created during the device degradation. The size of created ion diffusion path (25 μm) is similar to that of dark spot in Figure 4.14(e). Thus, we could conclude that the diffusion of Br^- and MA^+ is the direct evidence of SDPeLED degradation. And, the creation of diffusion path of Br^- and MA^+ was the direct source of EL decay.
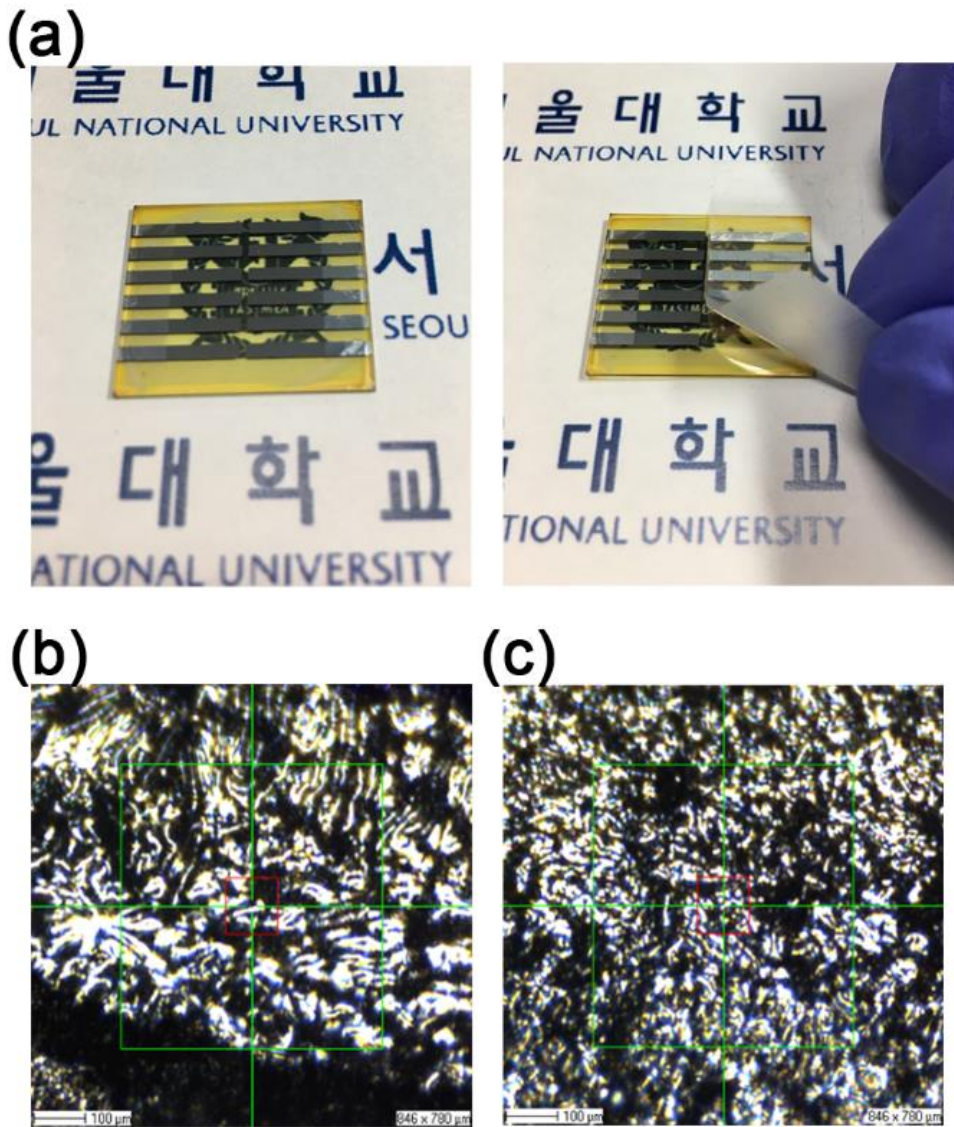
Figure 4.16 Experimental scheme of Al electrode peel-off. (a) Experimental scheme of peeling off process of Al electrode. Al electrode was peeled off by scotch tape. (b) Magnified image of peeled off Al electrode for unoperated device. (c) Magnified image of peeled off Al electrode for T_{10} device.

4.5.2   Analysis on the Peeled-off Al Electrode

In our previous report, we found that highly reactive metal-halide interaction induces more ion-diffusion from perovskite film which accelerates the degradation of perovskite solar cells.[70] The analysis on peeled off electrode was very efficient for investigation on degradation mechanism of perovskite solar cells.[40, 70] The diffused ions reacted with metal electrode and created metal-halide compounds or accumulated halide ion by-products. The experimental scheme of Al electrode peeling off is shown in Figure 4.16(a). Figure 4.16(b) and (c) are the magnified image of peeled off Al electrode for unoperated and T_{10} devices. For the red centered area (100 μm x 100 μm), TOF-SIMS surface profiling of peeled off Al electrode was conducted. Because the surface of Al electrodes was very rough with many wrinkles, we normalized the detected Al element of both samples for quantitative comparison. Interestingly, considerable Br^- and CN^- (MA^+) ions were detected in case of unoperated Al electrode (Figure 4.17). This observation implies that the degradation of SDPeLEDs had been processed since the evaporation of Al electrode was completed. Moreover, the comparison of Br^- and CN^- (MA^+) ions between unoperated and T_{10} electrodes indicates that both ions were diffused much more in case of device operation. The forward biased operation of SDPeLED accelerated ion diffusion from light-emission layer to Al electrode, resulting in rapid luminance decay of SDPeLED. The ion diffusion from perovskite layer indicates that the chemical structure of partial perovskite was deteriorated. This implies the possibility of morphological distortion of perovskite film. To investigate morphological change by device operation, TPBi
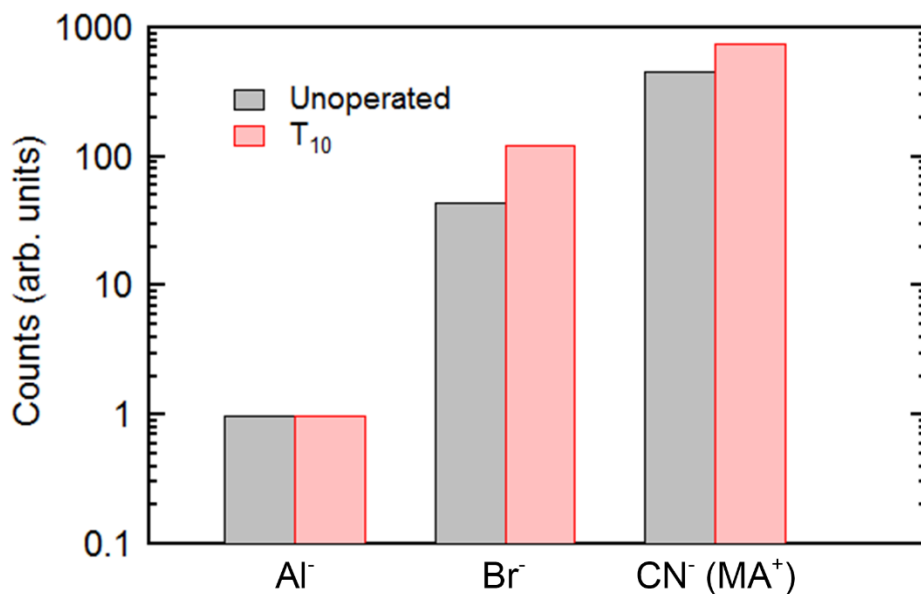
Figure 4.17 Analysis on the peeled off Al electrode. Ion distribution counts by TOF-SIMS surface profiling on peeled off Al electrodes.

film was additionally washed out after Al electrode peeling off. The Al electrode peeled off device was dipped into chloroform (CF) solvent for 30 s. This method of dissolving organic layer is very mild which have no physical damage to beneath perovskite film.[40] The initial perovskite film has very compact and dense film formation (Figure 4.18(a)). However, the perovskite film beneath Al electrode and TPBi without any current bias showed morphological distortion (Figure 4.18(b)). Perovskite grains were partially aggregated and fused which formed the grain size larger than 200 nm. Because it is the perovskite film of the unoperated device, we speculate that the ion diffusion from perovskite film to Al electrode was processed and distorted the film morphology. As we double checked from Figure 4.17, we could confirm that the degradation of SDPeLEDs had been processed right after the completion of the device fabrication. Figure 4.18(c) shows the morphology of T_{10}

perovskite film beneath TPBi and Al electrode. The aggregations of perovskite grains were increased and pin-holes were created. This pin-holes act as a shunt path between PEDOT:PSS and TPBi which reduce EL performance. Thus, the ion diffusion by device degradation induces morphological distortion of perovskite film, resulting in aggregation of perovskite grains, increased perovskite grain size, and creation of pin-holes.
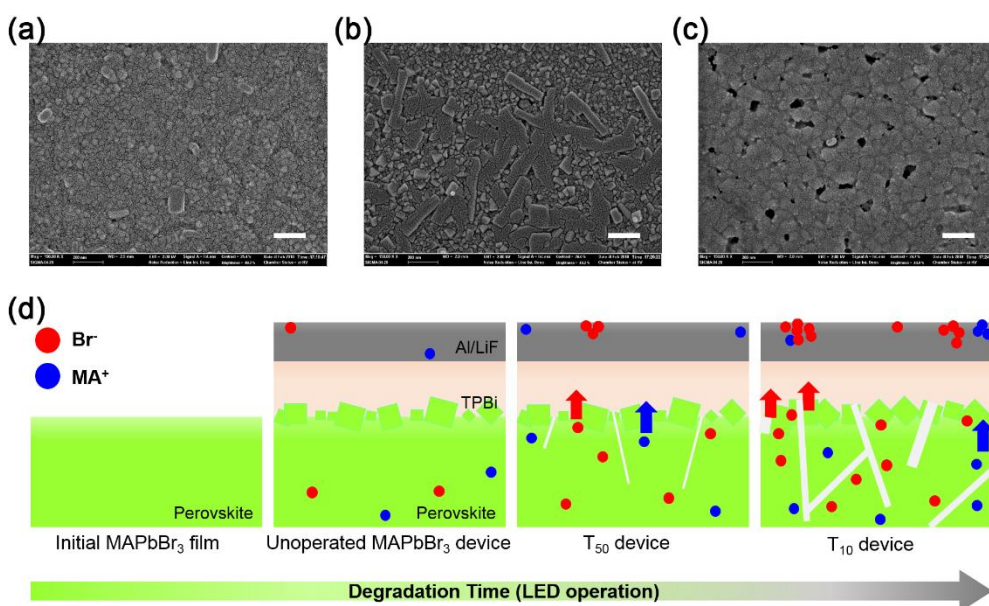
Figure 4.18 Morphological change of perovskite layer and degradation mechanism of SDPeLEDs. (a) SEM image of initial perovskite film. (b) SEM image of perovskite film from unoperated device. From the unoperated SDPeLED, Al electrode was peeled off and TPBi was washed out by dipping in CF. (c) SEM image of perovskite film from T_{10} device. From the T_{10} SDPeLED, Al electrode was peeled off and TPBi was washed out by dipping in CF. Scale bar is 200 nm in all images. (d) Ion diffusion induced degradation mechanism of SDPeLEDs. Red and blue dots indicate Br$^-$ and MA$^+$ ions.

4.6　Operational Degradation Mechanism of Perovskite Light-Emitting Diodes

Based on fore-mentioned observations, we found the direct evidence of SDPeLED degradation by constant current bias. The Br^- and MA^+ ions started to diffuse right after the completion of the SDPeLED fabrication. The device operation under forward bias over 3 *V* accelerated ion diffusion from perovskite layer which caused distortion of perovskite morphology. Chu et al. found that the degradation of perovskite begins with the whole grains and grain boundary not from the only grain boundary.[71] This observation is consistent with our results with the film morphology degradation. Figure 4.18(d) shows the degradation mechanism of SDPeLEDs. By innate ion diffusion from perovskite layer to Al electrode, perovskite film underwent morphological distortion. The aggregated grains might prohibit efficient radiative electron-hole recombination which decreases the EL performances. Constant current bias induced more aggregated perovskite grains and pin-holes which further decreases EL performance. As a result of the ion diffusion, the diffusion paths of Br^- and MA^+ were created which was the origin of the dark spot of SDPeLEDs.

4.7   Summary

We developed novel perovskite film fabrication method. Sequential deposition process of perovskite layer ensures compact and pin-hole free perovskite film and small perovskite grain size (less than 50 nm). Our device exhibited high luminance over 67,000 cd/m^2. This implies that SDPeLED is very robust under applied electric field that endures high applied current over 1000 mA/cm^2. Sturdy property of sequentially deposited perovskite film may come from the inorganic excess
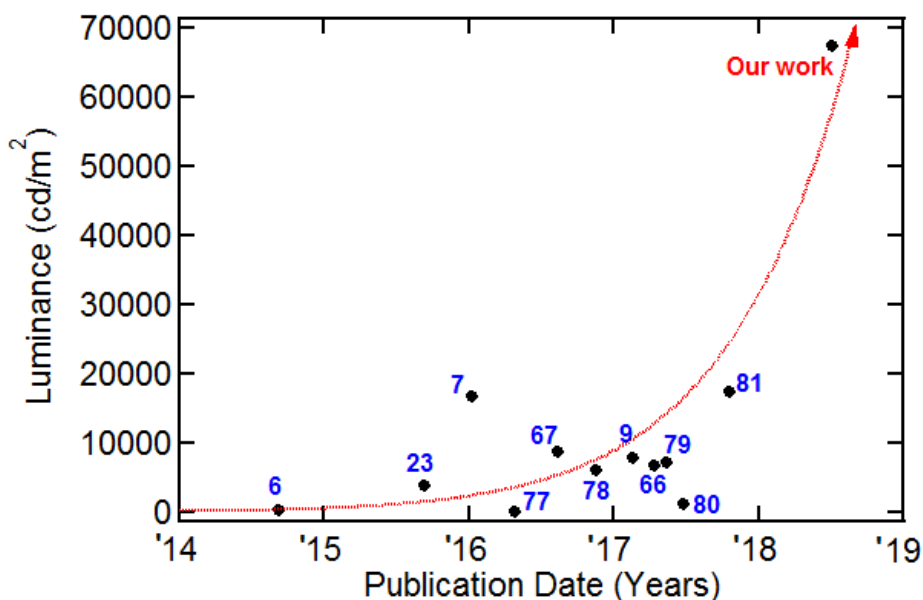
Figure 4.19 Reported luminance table of MAPbBr$_3$ LEDs by publication date**.**

compounds PbBr$_2$ - confirmed in XRD (Figure 4.2(c)). While maximum luminance of our SDPeLED shows extremely high value compare to other reported PeLEDs (Table 4.6, Figure 4.19), EQE and CE shows relatively lower values than that of record high reports. The entire current with respect to applied voltage shows relatively

81

higher value than that of reported record high PeLEDs.[9, 72] This also indicates leakage current of our SDPeLEDs is higher than that of record high PeLEDs. Leakage current may originate from various sources such as electron-hole injection imbalance, shunt path between ETL and HTL by pin-holes, or defect states in the perovskite layer.[3, 38, 73-75] We speculate that enhancement in charge imbalance and perovskite surface passivation have an effect on reducing leakage current. Cho et al. reported that the surface passivation between perovskite layer and ETL by TPBi mixed solvent pinning process reduces leakage current.[7] Wang et al. reduced leakage current by passivating perovskite surface with benzyl-amine in perovskite solar cells.[76] These reports imply that the further passivation of perovskite surface can reduce the leakage current. Thus, further study about reducing leakage current to increase EQE and CE will be conducted in our future work.

Table 4.6 MAPbBr$_3$ film type efficiency and lifetime table.

Publication date	Max. CE (cd/A)	Max. EQE (%)	Max. luminance (cd/m^2)	Lifetime	Ref.
	8.94	2.02	67,557	13 min @ T$_{50}$, 1000 cd/m^2	Our work
2014. 8. 3	0.3	0.1	364	-	[6]
2015. 8. 6	0.74	0.165	4,064	4 min @ T$_{66}$, 300 cd/m2	[23]
2015. 12. 4	42.9	8.53	16,936	-	[7]
2016. 3 .21	0.12	0.06	196	20 min @ T$_{50}$, 11 V	[77]
2016. 7. 08	5.1	-	8,794	20 s @ T$_{50}$, 1000 cd/m^2	[67]
2016. 10. 13	15.26	3.38	6,124	-	[78]
2017. 1. 16	17.1	9.3	8,000	45 min @ T$_{50}$, 3 mA/cm^2	[9]
	0.09	0.03	-	5 min @ T$_{60}$, 10 mA/cm^2	
2017. 3. 9	34.46	8.21	6,950	100 s @ T$_{50}$, 6.5 V	[66]
2017. 4. 7	9.45	2.28	7,263	-	[79]
2017. 5. 19	6.5	1.88	1,427	-	[80]
2017. 9. 15	29.0	7.26	17,630	25 min @ T$_{50}$, 2500 cd/m^2	[81]

We also investigated the device stability under continuous operation. The Br^- and MA^+ ion diffusion from perovskite layer to Al electrode was the direct evidence of the SDPeLED degradation. Because the ion diffusion in perovskite based optoelectronic devices during the device degradation is the innate characteristic, method to block external degradation sources (oxygen, humidity) such as encapsulation has the limitation to delay the degradation. Two strategies can be suggested to delay the degradation of PeLEDs. The first one is the insertion of ion diffusion blocking layer to the device. According to Tsang et al., the insertion of 8-hydroxyquinolatolithium (Liq) to the organic light-emitting diodes enhanced device lifetime.[82] The deposition of thin layer of Al_2O_3 on top of perovskite layer is supposed to block ion diffusion from perovskite layer.[83] The second one is the chemical compositional change of perovskite. In the perovskite solar cells, the incorporation of small amount of cesium to perovskite showed very stable device stability.[17] The introduction of 2D layered perovskite would enhance the device stability.[84-85] Moreover, we observed that SDPeLED didn't operate under exposure to ambient air (Figure 4.20). Under air exposure, perovskite film degrades not as much break the device operation. Kim et al. reported the XRD peak of perovskite film was not changed with respect to the air exposure time. And film color also was not changed.[60] Because the degradation of perovskite film was considered not to be the main degradation source under air exposure, the interfacial degradation should be investigated such as interface between electrode and charge transporting layer. Thus, the study of interfacial layer to block ion diffusion and compositional change of

84
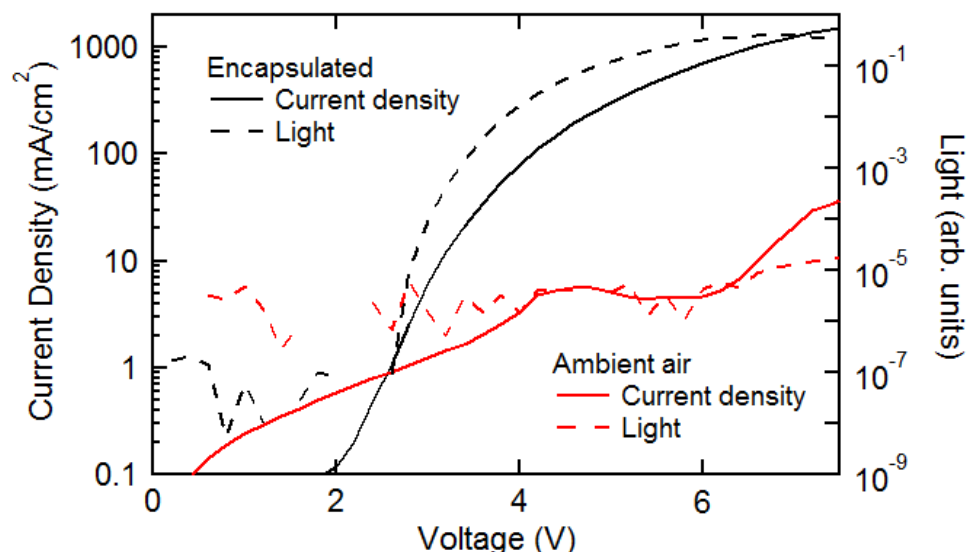
Figure 4.20 SDPeLED operation under ambient air without device encapsulation. SDPeLED shows non-idealistic diode curve under exposure to humidity and oxygen. The light-emission from perovskite layer was significantly diminished (4 order). The interaction between perovskite and Al electrode is speculated as an origin of device degradation.

perovskite layer to enhance the device stability will be our future work. Additionally, the effect of metal electrode to device stability of PeLEDs would be interesting.

In summary, we introduced sequential deposition method to fabricate perovskite film. The sequentially deposited perovskite layer showed compact and pin-hole free film. Based on high quality perovskite film, we fabricated very efficient and pure colored PeLEDs. Moreover, we found the direct evidence of the SDPeLED degradation. The ion diffusion from perovskite had electro-chemical interactions during device degradation. Based on quantitative observation, we proposed novel degradation mechanism of SDPeLEDs.

Chapter 5

Conclusion

In this thesis, degradation mechanism of perovskite optoelectronic devices was investigated. Direct evidence of ion-diffusion induced degradation sources was observed and analyzed. The similar degradation mechanism for both PSCs and PeLEDs suggests the direction for the further improvement of device lifetime.

$MAPbI_3$ PSCs showed iodide ion diffusion induced device degradation. In the first part, metal-ETL interface related interfacial degradation mechanism of inverted PSCs was investigated. The Ag electrode restoration process was introduced. The old Ag electrode was detached by tape and re-evaporated on the same area. As a result, PCE of new electrode was recovered. The degradation sources were detected by TOF-SIMS depth profiling. The diffusion and accumulation of iodide and sulfide ion from the perovskite layer to the Ag electrode were the origin of the device degradation. By performing Ag electrode restoration process, defect states were effectively removed

which led the recovery of PCE. The unique behavior of solar cell parameters (J_{SC}, V_{OC}, and FF) depend on the degradation time and Ag restoration process was analyzed by low temperature studies. Light intensity based activation energy analysis explained the trends of J_{SC} and FF. Energetic disorder explained the trend of V_{OC}. As a result, the unique degradation mechanism of inverted PSCs was suggested.

In the second part, highly bright and efficient PeLEDs were fabricated by sequential deposition method. The optimized device fabrication condition was acquired by varying the concentration of $PbBr_2$, MABr, PVP solutions, and perovskite film annealing time. The device exhibited 2.02% EQE and over 67,000 cd/m^2 luminance. However, the operational device lifetime was only 13 min (T_{50} lifetime). $MAPbBr_3$ PeLEDs showed bromide and MA^+ ion diffusion induced device degradation. The forward bias applied current accelerated ion diffusion during the device operation. The growth of dark spots followed facilitated diffusion model which implies the degradation sources originate from the ion diffusion. The diffusion of bromide and MA^+ ions were the direct evidence of PeLED degradation which was confirmed by TOF-SIMS depth profiling. The morphological investigation on the perovskite film before and after the device operation explained the process of the device degradation by forming of aggregated perovskite grains and creation of the pin-holes. Based on the observations, the unique degradation mechanism of SDPeLEDs was proposed.

In conclusion, this thesis provides electro-chemical analysis tools to investigate device physics for the perovskite optoelectronic devices. Low temperature analysis on the PSC would give powerful characterization method on the analysis of each solar cell parameters (J_{SC}, V_{OC}, FF) regarding the degradation time. Moreover, investigation on the elemental distribution by TOF-SIMS will be very useful to analyze the ion-diffusion induced device degradation. We believe our powerful analysis tools and

novel scientific findings on the degradation mechanism of perovskite optoelectronic device would contribute to the further improvement of perovskite optoelectronic devices.

Bibliography

[1] A. Kojima, K. Teshima, Y. Shirai, T. Miyasaka, *J. Am. Chem. Soc.* **2009**, 131, 6050.

[2] H.-S. Kim, C.-R. Lee, J.-H. Im, K.-B. Lee, T. Moehl, A. Marchioro, S.-J. Moon, R. Humphry-Baker, J.-H. Yum, J. E. Moser, M. Grätzel, N.-G. Park, *Sci. Rep.* **2012**, 2, 591.

[3] G. E. Eperon, V. M. Burlakov, P. Docampo, A. Goriely, H. J. Snaith, *Adv. Funct. Mater.* **2014**, 24, 151.

[4] J. Burschka, N. Pellet, S.-J. Moon, R. Humphry-Baker, P. Gao, M. K. Nazeeruddin, M. Grätzel, *Nature* **2013**, 499, 316.

[5] N. J. Jeon, J. H. Noh, Y. C. Kim, W. S. Yang, S. Ryu, S. I. Seok, *Nat. Mater.* **2014**, 13, 897.

[6] Z.-K. Tan, R. S. Moghaddam, M. L. Lai, P. Docampo, R. Higler, F. Deschler, M. Price, A. Sadhanala, L. M. Pazos, D. Credgington, F. Hanusch, T. Bein, H. J. Snaith, R. H. Friend, *Nat. Nanotechnol.* **2014**, 9, 687.

[7] H. Cho, S.-H. Jeong, M.-H. Park, Y.-H. Kim, C. Wolf, C.-L. Lee, J. H. Heo, A. Sadhanala, N. Myoung, S. Yoo, S. H. Im, R. H. Friend, T.-W. Lee, *Science* **2015**, 350, 1222.

[8]   X. Yang, X. Zhang, J. Deng, Z. Chu, Q. Jiang, J. Meng, P. Wang, L. Zhang, Z. Yin, J. You, *Nat. Commun.* **2018**, 9, 570.

[9]   Z. Xiao, R. A. Kerner, L. Zhao, N. L. Tran, K. M. Lee, T.-W. Koh, G. D. Scholes, B. P. Rand, *Nat. Photonics* **2017**, 11, 108.

[10] J. Si, Y. Liu, Z. He, H. Du, K. Du, D. Chen, J. Li, M. Xu, H. Tian, H. He, D. Di, C. Lin, Y. Cheng, J. Wang, Y. Jin, *ACS Nano* **2017**, 11, 11100.

[11] X. Deng, X. Wen, C. F. J. Lau, T. Young, J. Yun, M. A. Green, S. Huang, A. W. Y. Ho-Baillie, *J. Mater. Chem. C* **2016**, 4, 9060.

[12] Y. Yuan, T. Li, Q. Wang, J. Xing, A. Gruverman, J. Huang, *Science Advances* **2017**, 3.

[13] H. J. Snaith, A. Abate, J. M. Ball, G. E. Eperon, T. Leijtens, N. K. Noel, S. D. Stranks, J. T.-W. Wang, K. Wojciechowski, W. Zhang, *J. Phys. Chem. Lett.* **2014**, 5, 1511.

[14] B. Li, Y. Li, C. Zheng, D. Gao, W. Huang, *RSC Advances* **2016**, 6, 38079.

[15] J. Yang, T. L. Kelly, *Inorg. Chem.* **2017**, 56, 92.

[16] J. H. Noh, S. H. Im, J. H. Heo, T. N. Mandal, S. I. Seok, *Nano Lett.* **2013**, 13, 1764.

[17] M. Saliba, T. Matsui, J.-Y. Seo, K. Domanski, J.-P. Correa-Baena, M. K. Nazeeruddin, S. M. Zakeeruddin, W. Tress, A. Abate, A. Hagfeldt, M. Gratzel, *Energy Environ. Sci.* **2016**, 9, 1989.

[18] J. You, L. Meng, T.-B. Song, T.-F. Guo, Y. Yang, W.-H. Chang, Z. Hong, H. Chen, H. Zhou, Q. Chen, Y. Liu, N. De Marco, Y. Yang, *Nat. Nanotechnol.* **2015**, 11, 75.

[19] K. O. Brinkmann, J. Zhao, N. Pourdavoud, T. Becker, T. Hu, S. Olthof, K. Meerholz, L. Hoffmann, T. Gahlmann, R. Heiderhoff, M. F. Oszajca, N. A. Luechinger, D. Rogalla, Y. Chen, B. Cheng, T. Riedl, *Nature Commun.* **2017**, 8,

13938.

[20] Z. Jiang, X. Chen, X. Lin, X. Jia, J. Wang, L. Pan, S. Huang, F. Zhu, Z. Sun, *Sol. Energy Mater. Sol. Cells* **2016**, 146, 35.

[21] J. Zhao, X. Zheng, Y. Deng, T. Li, Y. Shao, A. Gruverman, J. Shield, J. Huang, *Energy Environ. Sci.* **2016**, 9, 3650.

[22] F. Zhang, X. Yang, M. Cheng, W. Wang, L. Sun, *Nano Energy* **2016**, 20, 108.

[23] J. Li, S. G. R. Bade, X. Shan, Z. Yu, *Adv. Mater.* **2015**, 27, 5196.

[24] H. Tan, A. Jain, O. Voznyy, X. Lan, F. P. García de Arquer, J. Z. Fan, R. Quintero-Bermudez, M. Yuan, B. Zhang, Y. Zhao, F. Fan, P. Li, L. N. Quan, Y. Zhao, Z.-H. Lu, Z. Yang, S. Hoogland, E. H. Sargent, *Science* **2017**, 355, 722.

[25] S. S. Shin, E. J. Yeom, W. S. Yang, S. Hur, M. G. Kim, J. Im, J. Seo, J. H. Noh, S. I. Seok, *Science* **2017**, 356, 167.

[26] S. D. Stranks, G. E. Eperon, G. Grancini, C. Menelaou, M. J. P. Alcocer, T. Leijtens, L. M. Herz, A. Petrozza, H. J. Snaith, *Science* **2013**, 342, 341.

[27] H. Chen, *Adv. Funct. Mater.* **2017**, 27, 1605654.

[28] M. A. Green, A. Ho-Baillie, H. J. Snaith, *Nat Photonics* **2014**, 8, 506.

[29] E. Mosconi, J. M. Azpiroz, F. De Angelis, *Chem. Mater.* **2015**, 27, 4885.

[30] Y. Han, S. Meyer, Y. Dkhissi, K. Weber, J. M. Pringle, U. Bach, L. Spiccia, Y.-B. Cheng, *J. Mater. Chem. A* **2015**, 3, 8139.

[31] J. Yang, B. D. Siempelkamp, D. Liu, T. L. Kelly, *ACS Nano* **2015**, 9, 1955.

[32] T. Leijtens, G. E. Eperon, S. Pathak, A. Abate, M. M. Lee, H. J. Snaith, *Nature Commun.* **2013**, 4, 2885.

[33] X. Zheng, B. Chen, J. Dai, Y. Fang, Y. Bai, Y. Lin, H. Wei, Xiao C. Zeng, J. Huang, *Nature Energy* **2017**, 2, 17102.

[34] A. B. Huang, J. T. Zhu, J. Y. Zheng, Y. Yu, Y. Liu, S. W. Yang, S. H. Bao, L. Lei, P. Jin, *J. Mater. Chem. C* **2016**, 4, 10839.

[35] J. You, L. Meng, T.-B. Song, T.-F. Guo, Y. Yang, W.-H. Chang, Z. Hong, H. Chen, H. Zhou, Q. Chen, Y. Liu, N. De Marco, Y. Yang, *Nat. Nanotechnol.* **2016**, 11, 75.

[36] C.-Z. Li, C.-C. Chueh, F. Ding, H.-L. Yip, P.-W. Liang, X. Li, A. K. Y. Jen, *Adv. Mater.* **2013**, 25, 4425.

[37] C. D. Weber, C. Bradley, M. C. Lonergan, *J. Mater. Chem. A* **2014**, 2, 303.

[38] J. Xu, A. Buin, A. H. Ip, W. Li, O. Voznyy, R. Comin, M. Yuan, S. Jeon, Z. Ning, J. J. McDowell, P. Kanjanaboos, J.-P. Sun, X. Lan, L. N. Quan, D. H. Kim, I. G. Hill, P. Maksymovych, E. H. Sargent, *Nature Commun.* **2015**, 6, 7081.

[39] H. Back, G. Kim, J. Kim, J. Kong, T. K. Kim, H. Kang, H. Kim, J. Lee, S. Lee, K. Lee, *Energy Environ. Sci.* **2016**, 9, 1258.

[40] J. Li, Q. Dong, N. Li, L. Wang, Adv. Energy Mater. **2017**, 7, 1602922.

[41] G. Abdelmageed, L. Jewell, K. Hellier, L. Seymour, B. Luo, F. Bridges, J. Z. Zhang, S. Carter, *Appl. Phys. Lett.* **2016**, 109, 233905.

[42] Q.-D. Dao, R. Tsuji, A. Fujii, M. Ozaki, *Organic Electronics* **2017**, 43, 229.

[43] M. E. Ziffer, J. C. Mohammed, D. S. Ginger, *ACS Photonics* **2016**, 3, 1060.

[44] I. Riedel, J. Parisi, V. Dyakonov, L. Lutsen, D. Vanderzande, J. C. Hummelen, *Adv. Funct. Mater.* **2004**, 14, 38.

[45] H. Cha, J. Wu, A. Wadsworth, J. Nagitta, S. Limbu, S. Pont, Z. Li, J. Searle, M. F. Wyatt, D. Baran, J.-S. Kim, I. McCulloch, J. R. Durrant, Adv. Mater. **2017**, 1701156.

[46] J. C. Blakesley, D. Neher, *Phys. Rev. B* **2011**, 84, 075210.

[47] Y. Shao, Y. Yuan, J. Huang, *Nature Energy* **2016**, 1, 15001.

[48] J. Kim, H. Jung, J. Song, K. Kim, C. Lee, *ACS Appl. Mater. Interfaces* **2017**, 9, 24052.

[49] T. Heumueller, T. M. Burke, W. R. Mateker, I. T. Sachs-Quintana, K. Vandewal,

C. J. Brabec, M. D. McGehee, *Adv. Energy Mater.* **2015**, 5, 1500111.

[50] Z. Xiao, Q. Dong, C. Bi, Y. Shao, Y. Yuan, J. Huang, *Adv. Mater.* **2014**, 26, 6503.

[51] V. I. Arkhipov, E. V. Emelianova, P. Heremans, H. Bässler, *Phys. Rev. B* **2005**, 72, 235202.

[52] J. Nelson, *Phys. Rev. B* **2003**, 67, 155209.

[53] V. D. Mihailetchi, J. K. J. van Duren, P. W. M. Blom, J. C. Hummelen, R. A. J. Janssen, J. M. Kroon, M. T. Rispens, W. J. H. Verhees, M. M. Wienk, *Adv. Funct. Mater.* **2003**, 13, 43.

[54] W. S. Yang, B.-W. Park, E. H. Jung, N. J. Jeon, Y. C. Kim, D. U. Lee, S. S. Shin, J. Seo, E. K. Kim, J. H. Noh, S. I. Seok, *Science* **2017**, 356, 1376.

[55] S. Yakunin, L. Protesescu, F. Krieg, M. I. Bodnarchuk, G. Nedelcu, M. Humer, G. De Luca, M. Fiebig, W. Heiss, M. V. Kovalenko, *Nature Commun.* **2015**, 6, 8056.

[56] X. Y. Chin, D. Cortecchia, J. Yin, A. Bruno, C. Soci, *Nature Commun.* **2015**, 6, 7383.

[57] G. Xing, N. Mathews, S. S. Lim, N. Yantara, X. Liu, D. Sabba, M. Grätzel, S. Mhaisalkar, T. C. Sum, *Nat. Mater.* **2014**, 13, 476.

[58] N.-G. Park, *Materials Today* **2015**, 18, 65.

[59] D. Shi, V. Adinolfi, R. Comin, M. Yuan, E. Alarousu, A. Buin, Y. Chen, S. Hoogland, A. Rothenberger, K. Katsiev, Y. Losovyj, X. Zhang, P. A. Dowben, O. F. Mohammed, E. H. Sargent, O. M. Bakr, *Science* **2015**, 347, 519.

[60] Y.-H. Kim, H. Cho, J. H. Heo, T.-S. Kim, N. Myoung, C.-L. Lee, S. H. Im, T.-W. Lee, *Adv. Mater.* **2015**, 27, 1248.

[61] H. Lee, C. Lee, *Adv. Energy Mater.* **2018**, 8, 1702197,.

[62] C. Eames, J. M. Frost, P. R. F. Barnes, B. C. O'Regan, A. Walsh, M. S. Islam,

Nature Commun. **2015**, 6, 7497.

[63] A. Miyata, A. Mitioglu, P. Plochocka, O. Portugall, J. T.-W. Wang, S. D. Stranks, H. J. Snaith, R. J. Nicholas, *Nat. Phys.* **2015**, 11, 582.

[64] Z. Yang, A. Surrente, K. Galkowski, N. Bruyant, D. K. Maude, A. A. Haghighirad, H. J. Snaith, P. Plochocka, R. J. Nicholas, *J. Phys. Chem. Lett.* **2017**, 8, 1851.

[65] H. Zhu, Y. Fu, F. Meng, X. Wu, Z. Gong, Q. Ding, M. V. Gustafsson, M. T. Trinh, S. Jin, X. Y. Zhu, *Nat. Mater.* **2015**, 14, 636.

[66] J.-W. Lee, Y. J. Choi, J.-M. Yang, S. Ham, S. K. Jeon, J. Y. Lee, Y.-H. Song, E. K. Ji, D.-H. Yoon, S. Seo, H. Shin, G. S. Han, H. S. Jung, D. Kim, N.-G. Park, *ACS Nano* **2017**, 11, 3311.

[67] Z. Wang, T. Cheng, F. Wang, S. Dai, Z. a. Tan, *Small* **2016**, 12, 4412.

[68] C. Gärditz, A. Winnacker, F. Schindler, R. Paetzold, *Appl. Phys. Lett.* **2007**, 90, 103506.

[69] A. Guerrero, J. You, C. Aranda, Y. S. Kang, G. Garcia-Belmonte, H. Zhou, J. Bisquert, Y. Yang, *ACS Nano* **2016**, 10, 218.

[70] H. Lee, C. Lee, *Adv. Energy Mater.* **2018**, 8, 1702197.

[71] Z. Chu, M. Yang, P. Schulz, D. Wu, X. Ma, E. Seifert, L. Sun, X. Li, K. Zhu, K. Lai, *Nature Commun.* **2017**, 8, 2230.

[72] L. Zhang, X. Yang, Q. Jiang, P. Wang, Z. Yin, X. Zhang, H. Tan, Y. Yang, M. Wei, B. R. Sutherland, E. H. Sargent, J. You, *Nature Commun.* **2017**, 8, 15640.

[73] X. Dai, Z. Zhang, Y. Jin, Y. Niu, H. Cao, X. Liang, L. Chen, J. Wang, X. Peng, *Nature* **2014**, 515, 96.

[74] J. Lim, M. Park, W. K. Bae, D. Lee, S. Lee, C. Lee, K. Char, *ACS Nano* **2013**, 7, 9019.

[75] W. Nie, H. Tsai, R. Asadpour, J.-C. Blancon, A. J. Neukirch, G. Gupta, J. J.

Crochet, M. Chhowalla, S. Tretiak, M. A. Alam, H.-L. Wang, A. D. Mohite, *Science* **2015**, 347, 522.

[76] F. Wang, W. Geng, Y. Zhou, H.-H. Fang, C.-J. Tong, M. A. Loi, L.-M. Liu, N. Zhao, *Adv. Mater.* **2016**, 28, 9986.

[77] Z.-F. Shi, X.-G. Sun, D. Wu, T.-T. Xu, S.-W. Zhuang, Y.-T. Tian, X.-J. Li, G.-T. Du, *Nanoscale* **2016**, 8, 10035.

[78] X. Zhao, B. Zhang, R. Zhao, B. Yao, X. Liu, J. Liu, Z. Xie, *J. Phys. Chem. Lett.* **2016**, 7, 4259.

[79] P. Chen, Z. Xiong, X. Wu, M. Shao, X. Ma, Z.-h. Xiong, C. Gao, *J. Phys. Chem. Lett.* **2017**, 8, 1810.

[80] F. Meng, C. Zhang, D. Chen, W. Zhu, H.-L. Yip, S.-J. Su, *J. Mater. Chem. C* **2017**, 5, 6169.

[81] X.-F. Peng, X.-Y. Wu, X.-X. Ji, J. Ren, Q. Wang, G.-Q. Li, X.-H. Yang, *J. Phys. Chem. Lett.* **2017**, 8, 4691.

[82] D. P.-K. Tsang, T. Matsushima, C. Adachi, *Sci. Rep.* **2016**, 6, 22463.

[83] D. Koushik, W. J. H. Verhees, Y. Kuang, S. Veenstra, D. Zhang, M. A. Verheijen, M. Creatore, R. E. I. Schropp, *Energy Environ. Sci.* **2017**, 10, 91.

[84] H. Tsai, W. Nie, J.-C. Blancon, C. C. Stoumpos, R. Asadpour, B. Harutyunyan, A. J. Neukirch, R. Verduzco, J. J. Crochet, S. Tretiak, L. Pedesseau, J. Even, M. A. Alam, G. Gupta, J. Lou, P. M. Ajayan, M. J. Bedzyk, M. G. Kanatzidis, A. D. Mohite, *Nature* **2016**, 536, 312.

[85] H. Tsai, W. Nie, J.-C. Blancon, C. C. Stoumpos, C. M. M. Soe, J. Yoo, J. Crochet, S. Tretiak, J. Even, A. Sadhanala, G. Azzellino, R. Brenes, P. M. Ajayan, V. Bulović, S. D. Stranks, R. H. Friend, M. G. Kanatzidis, A. D. Mohite, *Adv. Mater.* **2018**, 1704217.

Publication

[1] International Journals

1. **H. Lee** and C. Lee, "Analysis of Ion-Diffusion-Induced Interface Degradation in Inverted Perovskite Solar Cells via Restoration of the Ag Electrode", Adv. Energy Mater., **8**, 1702197 (2018) **"Front cover"**

2. **H. Lee**, P. Tyagi, S. Rhee, M. Park, J. Song, J. Kim, and C. Lee, "Analysis of Photovoltaic Properties of a Perovskite Solar Cell: Impact of Recombination, Space Charge, Exciton, and Disorder", *IEEE J. Photovolt.*, **7**, 1681 (2017)

3. **H. Lee**, J. Sohn, P. Tyagi, and C. Lee, "Crystallinity dependent thermal degradation in organic solar cell", *Appl. Phys. Lett.*, **110**, 53301 (2017)

4. P. Tyagi, A. Kumar, S. Rhee, **H. Lee**, J. Song, J. Kim, and C. Lee, "Plasmon-induced slow aging of exciton generation and dissociation for stable organic solar cells", *Optica*, **3**, 1115 (2016)

5. **H. Lee**, S. Rhee, J. Kim, C. Lee, and H. Kim, "Surface Coverage Enhancement of a Mixed Halide Perovskite Film by using an UV-Ozone Treatment", *J. Korean. Phys. Soc.*, **69**, 406 (2016)

6. S. In, D. Mason, **H. Lee**, M. Jung, C. Lee, and N. Park, "Enhanced Light Trapping and Power Conversion Efficiency in Ultrathin Plasmonic Organic Solar Cells: A Coupled Optical-Electrical Multi-physics Study on the Effect of Nanoparticle Geometry", *ACS Photon.*, **2**, 78 (2015)

[2] International Conferences

1. **H. Lee**, D. Ko, and C. Lee, "Analysis on Ion Diffusion Induced Degradation Mechanism of Sequentially Deposited Perovskite Light Emitting Diodes", The International Conference on Science and Technology of Synthetic Metals 2018 (ICSM 2018), Busan, Korea (July, 2018). *Oral presentation.*

2. **H. Lee** and C. Lee, "Unraveling the Ion Diffusion Induced Degradation Mechanism of Inverted Perovskite Solar Cells by Temperature Analysis", 2018 MRS Spring Meeting, Arizona, USA (Apr, 2018). *Oral presentation*.

3. **H. Lee** and C. Lee, "TEMPERATURE ANALYSIS ON DIRECT EVIDENCE OF INVERTED PEROVSKITE SOLAR CELL DEGRADTAION", Global Photovoltaic Conference 2018, Gwangju, Korea (Mar, 2018). *Oral presentation, selected as a GPVC 2018 Best Oral Presentation Award.*

4. **H. Lee** and C. Lee, "Straight forward evidence for long-term interfacial degradation of inverted perovskite solar cells", The 17th International Meeting on Information Display, Busan, Korea (Aug, 2017). ***Oral presentation, selected as an IMID 2017 awardee for KIDS awards bronze (3rd prize).***

5. **H. Lee**, K. An, S. Rhee, P. Tyagi, and C. Lee, "The effect of Liq layer on inverted perovskite solar cells; working mechanism & stability analysis", 2017 MRS Spring Meeting, Arizona, USA (Apr, 2017).

6. **H. Lee**, P. Tyagi, K. An, and C. Lee, "Improving fill factor and stability of inverted perovskite solar cells using Liq electron injection layer", Hybrid and Organic Photovoltaics 2016 (HOPV 16), Swansea, United Kingdom (Jul, 2016).

7. **H. Lee**, J. Sohn, J. Song, K. An, J. Kim, S. Rhee, J. Kim, P. Tyagi, and C. Lee, "The effect of thermal degradation in the inverted organic solar cells depend on the different crystalline polymers", The 16th International Meeting on Information Display (IMID 16), Jeju, Korea (Aug, 2016).

8. **H. Lee**, J. Kim, S. Rhee, H. Kim, and C. Lee, "Surface Coverage Enhancement of Mixed Halide Perovskite Film by UV-ozone Treatment", The 9th International Conference on Advanced Materials and Devices (ICAMD), Jeju, Korea (Dec, 2015).

9. **H. Lee**, J. Lim, J. Song, H. Song, H. Kim, I. Byun, K. An, S. Rhee, S. Lee, K. Char, and C. Lee, "CdSe tetrapod interfacial layer for improving electron extraction in planar hetero-junction perovskite solar cells", MRS Fall Meeting & Exhibit (MRS FALL 2015), Boston, Massachusetts, USA (Nov, 2015).

10. **H. Lee**, S. Rhee, J. Song, J. Kim, and C. Lee, "The effects of humidity and temperature to the perovskite film and its photovoltaic performances", 25th International Photovoltaic Science and Engineering Conference & Global Photovoltaic Conference 2015, Busan, Korea (Nov, 2015).

11. **H. Lee**, S. Rhee, J. Song, J. Kim, and C. Lee, "Effect of hole transport layer thickness on planar hetero-junction Perovskite solar cells", The 15th International Meeting on Information Display (IMID 15), Daegu, Korea (Aug, 2015).

12. **H. Lee**, H. Song, J. Song, M. Park, J. Kim, S. Rhee, and C. Lee, "Effect of Spiro-MeOTAD variation on planar hetero-junction Perovskite solar cells", Global Photovoltaic Conference 2014 (GPVC 2014), Busan, Korea (Nov, 2014).

13. **H. Lee**, J. Kim, H. Song, H. Shin, Y. Ko, J. Song, J. Kim, and C. Lee, "Surface Coverage Analysis of Planar Perovskite Solar Cell", Hybrid and Organic Photovoltaics 2014 (HOPV 14), Lausanne, Switzerland (May, 2014).

Abstract in Korean (한글 초록)

페로브스카이트는 차세대 광전소자로서 각광받는 물질이다. ABX$_3$ (A: larger cation, B: smaller cation, X: halide anion) 구조를 갖는 유기 무기 하이브리드 페로브스카이트는 구조의 차원에 따라 반도체 특성부터 금속 전이 특성까지 다양한 성질을 나타낸다. 페로브스카이트 구조의 2 차원에서 3 차원으로의 상 변이는 넓은 범위의 밴드 갭 변화를 보이며 광전 소자로 적용하는데 있어서 여러 광학, 전기적 특성을 제공한다. 이온화된 페로브스카이트의 결정은 높은 흡광 계수 (1.5x10^4 cm^{-1} at 550 nm for CH$_3$NH$_3$PbI$_3$)를 보이는데, 이는 550 nm 파장의 빛이 통과할 수 있는 박막의 두께가 0.66 μm 정도임을 나타낸다. 이런 우월한 흡광 특성은 페로브스카이트가 박막 태양전지에 적용 가능함을 시사한다. 2009 년 첫번째 페로브스카이트 태양전지가 보고된 이래로 태양전지의 전력 변환 효율은 빠르게 증가했다. 나아가 최근에는 페로브스카이트 태양전지가 실리콘 태양전지를 능가하는 차세대 지속 가능한 에너지원으로 여겨지고 있다. 게다가 페로브스카이트의 원소 조합 변경을 통한 밴드 갭의 조절 가능성은 발광 파장의 조절 가능성을 의미하며 페로브스카이트를 발광 다이오드 같은 여러 광원으로의 적용 가능함을 나타낸다. 실 예로, 페로브스카이트 발광다이오드의 발광 반치폭은 약 20 nm 로 특성이 매우 우수하다. 이러한 높은 색 순도는 유기발광다이오드 등의 상업화된 광원들에 비해 큰 강점이다.

페로브스카이트는 DMF, DMSO, 에탄올, 물 등 여러 극성 용매에 쉽게 분해되는 성질을 갖는다. 다습한 환경에서 페로브스카이트는 심각한 열화 과정을 겪는다. 페로브스카이트의 열화는 페로브스카이트를 기반으로 하는 광전소자들의 안정성과 수명을 저해한다. 차세대 에너지원 혹은 광원으로의 성공을 위해서는 페로브스카이트의 안정성 문제를 해결해야한다. 미량의 cesium 혹은 formamidinium 을 페로브스카이트에 첨가한 연구와 페로브스카이트의 구조적 발전 연구들이 페로브스카이트 광전소자들의 수명 안정성을 높이기 위해 보고되었다. 그럼에도 불구하고, 페로브스카이트 광전소자들을 소자들이 봉지 된 (encapsulated) 상태에서도 열화가 진행되었다. 따라서 열화의 원인과 그에 작용하는 열화 원리에 대한 체계적인 연구가 필요하다. 페로브스카이트 광전소자의 상업화를 위해서는 열화에 대한 연구가 선행되어야 한다.

본 논문에서는 페로브스카이트 태양전지 및 발광다이오드의 열화 원리에 대한 체계적인 연구가 논의되었다. 페로브스카이트 광전소자의 구조적인 부분에서는 역구조 (inverted structure)가 사용되었다. 역구조란 전자가 상단 금속 전극으로부터 주입 혹은 추출되며 정공이 하단의 투명 전극인 ITO 로부터 주입 혹은 추출되는 구조를 말한다.

첫번째 파트에서는 페로브스카이트 태양전지에 대해 기술하였다. 역구조 페로브스카이트 태양전지의 이온 확산에 의한 계면 열화의 직접적인 증거가 제시되었다. 1000 시간이 넘는 장 시간 소자 열화 기간 동안 페로브스카이트 태양전지는 전류 밀도와 fill factor 에서 큰 열화를 나타낸다. Ag 전극과 PCBM 사이의 계면 열화를 분석하기 위해 소자 열화 10, 20, 30, 40 일차에 Ag 전극을 물리적으로 제거하고 다시 전극을 증착하는 기법을 도입했다. Ag 전극의 재 증착을 통해 태양전지의 전력 변환 효율이 회복되는 현상을 볼 수 있었다. 전극 재 증착을 통해 태양전지의 개방

전압과 fill factor 가 복구되는 반면에 전류 밀도는 약간 감소하는 추세를 나타냈다. 전극 재증착에 따른 활성화에너지 (activation energy)의 감소는 fill factor 의 회복으로 나타났다. 페로브스카이트 태양전지의 열화의 결과로 인한 확산된 요오드 이온은 PCBM 분자들과 반응을 하며 PCBM 의 quasi n 도핑 효과를 보였다. 전극 재증착 과정에 따라 요오드 이온과 PCBM 분자들의 가역반응은 태양전지 전류 밀도의 변화와 관련이 있다. 저온 측정을 통한 energetic disorder 모델은 전극 재증착에 따른 태양전지의 개방 전압 증가를 설명하고있다. 마지막으로 제시된 재결합 구조하의 역구조 페로브스카이트 태양전지의 열화 메커니즘이 제시되었다.

두번째 파트에서는 페로브스카이트 발광다이오드에 대해 기술하였다. 페로브스카이트 발광다이오드 연구 분야에서 중요한 이슈는 조밀하고 핀홀 없는 페로브스카이트 박막을 형성하는 것이다. 본 논문에서는 연속 증착 방법을 페로브스카이트 박막 형성 과정에 도입했다. $PbBr_2$ 용액과 MABr 용액이 차례대로 스핀 코팅 되고 가열 되었으며 조밀하고 핀홀 없는 페로브스카이트 박막을 형성하는데 사용되었다. 그 결과 페로브스카이트 발광다이오드는 67,557 cd/m^2 의 휘도와 2.02%의 EQE 를 나타냈다. 효율적인 페로브스카이트 발광다이오드를 기반으로 열화의 원인에 대한 연구가 진행되었다. 발광다이오드 구동에 따른 이온 확산의 직접적 증거가 관찰되었으며 열화 원인과 Al 전극 사이의 전기 화학적 반응을 토대로 한 페로브스카이트 발광다이오드의 열화 메커니즘이 제시되었다.

본 학위 논문은 페로브스카이트 광전소자의 열화 메커니즘을 분석하기 위한 실용적 접근법을 다뤘다. 이온 확산을 기저로 한 금속 전극 계면에 대한 열화 메커니즘은 페로브스카이트 광전소자의 수명 안정성 발전에 기여를 할 것이라 기대된다.